Article

Immunity

A type I interferon-mitochondrial axis regulates efferocytosis and interferon-stimulated gene induction in macrophages

Graphical abstract

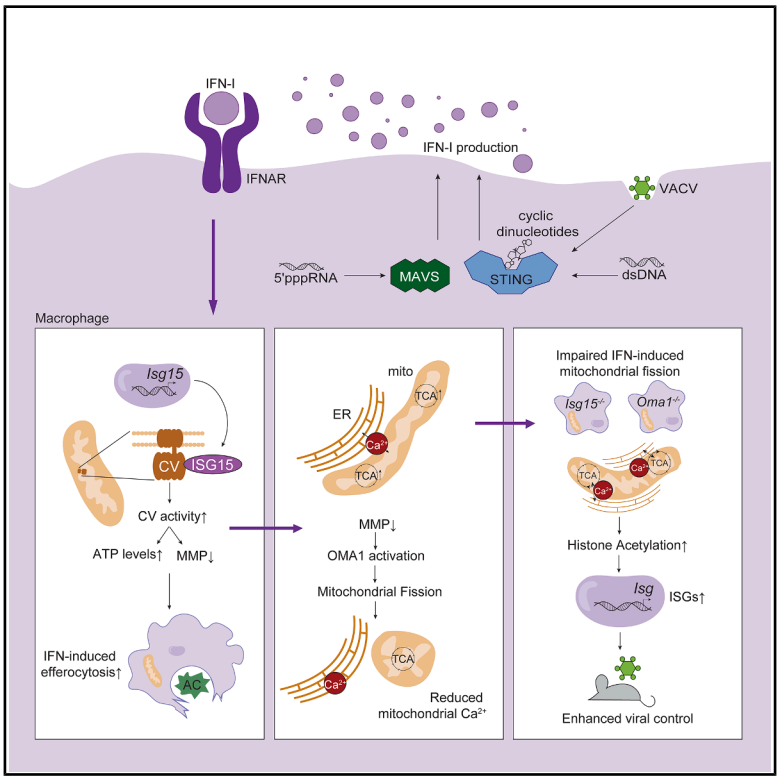

Highlights

- Cytosolic nucleic acid sensing does not trigger the Warburg effect in macrophages
- IFN-I decreases MMP in macrophages with intact OXPHOS
- ISGylation is required for reduction in MMP and IFN-induced efferocytosis
- Low MMP induces mitochondrial fission, limiting ISG induction via mitochondrial-ER contacts

Authors

Gillian Dunphy, Irene Adán-Barrientos, Irene Fernández-Delgado, ..., Susana Guerra, Francisco Sánchez-Madrid, David Sancho

Correspondence

gillian.dunphy@cnic.es (G.D.), dsancho@cnic.es (D.S.)

In brief

Cytosolic nucleic acid sensors contribute to pathogenic and autoinflammatory inflammation; however, little is known about the metabolic adaptations that they induce. Dunphy et al. find that these pathways induce type I interferon-dependent metabolic changes in macrophages, characterized by a decrease in mitochondrial membrane potential and increased mitochondrial fission, promoting efferocytosis, while restraining ISG induction to promote the resolution of inflammation.

Dunphy et al., 2026, Immunity *59*, 306–321
February 10, 2026 © 2025 The Authors. Published by Elsevier Inc.
https://doi.org/10.1016/j.immuni.2025.12.010

CellPress

CellPress
OPEN ACCESS

Immunity

Article

A type I interferon-mitochondrial axis regulates efferocytosis and interferon-stimulated gene induction in macrophages

Gillian Dunphy,[1,*] Irene Adán-Barrientos,[1,2,3] Irene Fernández-Delgado,[1,3] Carolina Villarroya-Beltri,[1,4] Ignacio Heras-Murillo,[1] Elena Moya-Ruiz,[1,3] Miguel Sánchez-Álvarez,[1,6] Aitor Jarit-Cabanillas,[1,2,3] Miguel A. del Pozo,[1] Susana Guerra,[7] Francisco Sánchez-Madrid,[1,5,8] and David Sancho[1,9,*]

[1]Centro Nacional de Investigaciones Cardiovasculares Carlos III (CNIC), 28029 Madrid, Spain
[2]Department of Immunology, Ophthalmology and ENT, School of Medicine, Universidad Complutense de Madrid, 28040 Madrid, Spain
[3]Escuela de Doctorado, Universidad Autónoma de Madrid, 28049 Madrid, Spain
[4]Centro de Biología Molecular Severo Ochoa, CSIC, 28049 Madrid, Spain
[5]Instituto de Investigación Sanitaria Hospital Universitario La Princesa, Universidad Autónoma de Madrid, 28006 Madrid, Spain
[6]Instituto de Investigaciones Biomédicas Sols-Morreale, CSIC-UAM, 28029 Madrid, Spain
[7]Department of Preventive Medicine, Public Health and Microbiology, Universidad Autónoma de Madrid, 28029 Madrid, Spain
[8]Centro de Investigación Biomédica en Red de Enfermedades Cardiovasculares (CIBERCV), 28029 Madrid, Spain
[9]Lead contact
*Correspondence: gillian.dunphy@cnic.es (G.D.), dsancho@cnic.es (D.S.)
https://doi.org/10.1016/j.immuni.2025.12.010

SUMMARY

Macrophage metabolism is intricately linked to cellular function. Contrasting with Toll-like receptor (TLR) stimulation, cytosolic nucleic acid sensing induced a decrease in mitochondrial membrane potential (MMP) while maintaining mitochondrial respiration. Interferon α/β (IFN-I) receptor (IFNAR) signaling was necessary and sufficient for this metabolic response. IFNAR signaling induced interferon-stimulated gene 15 (ISG15) expression and ISGylation of mitochondrial proteins, including subunits of mitochondrial complex V, increasing ATP production and decreasing MMP, thus enhancing macrophage efferocytic capacity. Moreover, the IFNAR-ISG15-mediated drop in MMP activated the mitochondrial protease OMA1, inducing mitochondrial fission and decreasing endoplasmic reticulum-mitochondria communication, thus dampening IFN-stimulated gene (ISG) induction. Loss of ISG15 or OMA1 enhanced histone acetylation and ISG induction upon IFN-I stimulation, in a manner dependent on mitochondrial calcium uptake. This increase in ISG induction provided protection against acute viral infections. These data indicate that IFNAR-ISG15 signaling boosts efferocytosis while limiting ISG induction, thereby promoting the resolution of inflammation.

INTRODUCTION

Macrophages are innate immune cells required for mammalian development, homeostasis, and pathogen clearance.[1] They act as tissue sentinels, sensing pathogen- and damage-associated molecular patterns through pattern recognition receptors (PRRs).[2] Ligation of these receptors activates signaling pathways that promote immune cell activation via epigenetic, transcriptional, and metabolic processes.[3,4] Metabolic changes in activated immune cells have been linked to their function, regulating cytokine production,[4–7] generation of reactive oxygen species (ROS),[8,9] migration,[10] and antimicrobial effects.[11] However, not all stimuli lead to the same metabolic response.[12] Although many studies have addressed the response to Toll-like receptor (TLR) agonists,[4,13] little is known about the metabolic adaptations downstream of cytosolic nucleic acid sensors.[14] Cytosolic nucleic acids activate stimulator of interferon genes (STING) and mitochondrial antiviral signaling protein (MAVS) to induce immune responses via cytokine production, especially type I interferons (IFN-I).[15–18] IFN-I, comprising IFN-α and IFN-β, are fundamental for immune system function.[19–24] They signal via the interferon α/β receptor (IFNAR), inducing IFN-stimulated genes (ISGs).[25] One such ISG is ISG15, a ubiquitin-like protein that has been implicated in antiviral immunity as well as the modulation of cellular metabolism.[26–28] The timely induction of IFNs and ISGs is essential for pathogen clearance and the resolution of inflammation.[29,30]

Cytosolic nucleic acid sensing is key in a variety of pathogenic and autoinflammatory contexts, yet the metabolic consequences of this response remain to be studied. We therefore compared the metabolic adaptations in macrophages in response to agonists of STING, MAVS, and several TLRs. Activation of cytosolic nucleic acid sensors led to macrophage activation without the block in mitochondrial respiration and switch to

 © 2025 The Authors. Published by Elsevier Inc.
This is an open access article under the CC BY-NC-ND license (http://creativecommons.org/licenses/by-nc-nd/4.0/).

glycolysis observed upon TLR stimulation, indicating an alternative metabolic reprogramming to meet the anabolic demands of immune activation. IFNAR signaling was both necessary and sufficient for the metabolic changes observed upon nucleic acid sensing in macrophages. IFNAR signaling upregulated ISG15, which conjugated to several mitochondrial targets, including complex V (CV). IFN-I treatment increased CV activity and thus ATP production in an ISG15-dependent manner, depleting mitochondrial membrane potential (MMP) in the cell, and thus promoting efferocytosis. In parallel, MMP depletion activated the mitochondrial protease OMA1, triggering mitochondrial fission and limiting ISG induction. Collectively, these observations suggest a feedback loop upon IFN-I detection to limit ISG induction and promote clearance of cellular debris.

RESULTS

Cytosolic nucleic acid sensors induce an IFN-I-driven metabolic response

To study metabolic changes upon STING activation, we transfected bone-marrow-derived macrophages (BMDMs) with cyclic di-guanosine monophosphate (c-di-GMP), a STING agonist and compared this to stimulation with lipopolysaccharide (LPS), a TLR4 agonist. Analysis of the oxygen consumption rate (OCR) showed that although LPS stimulation induced a decrease in the maximal respiratory rate (MRR) as described,[13] c-di-GMP-transfected BMDMs did not exhibit this reduction (Figures 1A and 1B). To confirm that this effect was not specific to c-di-GMP or to this specific concentration, we compared c-di-GMP with another STING agonist, 2′3′ cyclic GMP-AMP (cGAMP), at two concentrations. Neither STING agonist induced a decrease in OCR, and increasing concentrations of c-di-GMP and cGAMP even increased OCR (Figure S1A). Moreover, while lactate production increased upon TLR stimulation, this induction was lower following cytosolic nucleic acid sensing (Figure 1C). We next measured MMP in BMDMs upon activation. MMP is the driving force required for ATP production by the electron transport chain and has been associated with mitochondrial ROS production[31,32] and nuclear gene expression.[33] Treatment with STING or MAVS agonists decreased MMP, as measured by tetramethylrhodamine methyl ester (TMRM) staining, after 20 h, but not 4 h, whereas all TLR agonists increased MMP (Figure 1D).

A prominent feature of cytosolic nucleic acid sensors is high IFN-I induction.[34] Previous studies in myeloid cells observed diverse metabolic effects of IFN-I on metabolism, prompting us to test the effect of IFN-I on BMDMs.[23,35] Direct stimulation of BMDMs with IFN-α or IFN-β for 4 or 16 h recapitulated the decrease in MMP observed at later time points of STING stimulation (Figure 1E). Decreased MMP was confirmed using the ratiometric dye JC-1 (Figure S1B). Given the altered MMP, we quantified mitochondria upon IFN-I treatment using TOM20 and found an increase at 16 h post IFN-β stimulation (Figure S1C) and no change in cell viability (Figure S1D), indicating that the decrease in MMP was not due to mitochondrial loss or cell death. IFN-I stimulation induced no changes in OCR (Figures S1E and S1F). To determine whether metabolic differences between stimuli were driven by variations in IFN-I production, we measured IFN-β production 20 h after stimulation. All tested stimuli produced IFN-β to a similar extent (Figure S1G). This suggests that while both cytosolic nucleic acid sensing and TLR stimulation induce IFN-I production, only the former displays a decrease in MMP, concomitant with sustained mitochondrial respiration.

Macrophages stimulated with the TLR9 ligand CpG also showed a decrease in mitochondrial respiration, similar to LPS, in contrast to reports in plasmacytoid dendritic cells (pDCs) (Figures S1H–S1J).[23] To test whether the metabolic phenotype observed upon IFN-I stimulation was macrophage specific, we stimulated Flt3L dendritic cells (DCs) with IFN-β for 20 h. IFN-β led to decreased MMP in type 1 and type 2 conventional DCs (cDC1s and cDC2s, respectively) and pDCs; no detectable change in glucose uptake; and increased expression of major histocompatibility complex class II (MHC class II) and CD86 compared with untreated Flt3L DCs (Figure S1K). This indicates that the effect observed in BMDMs is not macrophage specific but occurs in other myeloid cells.

To test that the effect of IFN-I on macrophage metabolism occurs via IFNAR, we used an IFNAR-blocking antibody (anti-IFNAR) prior to stimulation with c-di-GMP, IFN-α, or carbonyl cyanide m-chlorophenyl hydrazone (CCCP). Notably, anti-IFNAR treatment prevented the loss of MMP observed upon c-di-GMP or IFN-I treatment but had no effect on the decrease in MMP induced by CCCP (Figure 1F). This anti-IFNAR treatment had no effect on *Ifnb* mRNA production after c-di-GMP stimulation but did decrease downstream expression of ISGs ISG15 and C-C motif chemokine ligand 5 (CCL5) (Figures S1L and S1M). We conclude that cytosolic nucleic acid sensing induces a distinct cellular metabolism compared with the canonical changes observed upon TLR stimulation and that IFN-I is both sufficient and required for these changes.

IFN-I promotes an ISG15-dependent drop in MMP that induces OMA1-dependent mitochondrial fission

Decreased MMP activates the mitochondrial protease OMA1.[36] OMA1 is a zinc metalloprotease localized to the inner mitochondrial membrane, which cleaves optic atrophy 1 (OPA1) to promote inner mitochondrial membrane fission.[37] We observed the mitochondrial morphology in BMDMs after stimulation with c-di-GMP or IFN-α, analyzing TOM20 staining using the MiNA plugin to calculate mitochondrial parameters.[38,39] The mean branch length indicates the average length of all mitochondria per cell, whereas the mitochondrial footprint quantifies the area of the cytoplasm occupied by mitochondria, with elongated mitochondria occupying more area and fragmented mitochondria occupying less. We observed a decrease in mitochondrial fragment size indicative of mitochondrial fission after 20 h of STING stimulation, which was phenocopied by IFN-α or CCCP treatment (Figures 2A and 2B). Analysis of transmission electron microscopy images[40] revealed a decrease in mitochondrial length and an increase in circularity, among other changes in morphology, consistent with increased mitochondrial fission upon IFN-I stimulation (Figure S2A).

These results suggested that mitochondrial fission occurs in BMDMs due to the decrease in MMP driven by IFN-I. To demonstrate whether OMA1 mediates the observed mitochondrial fission, we assessed the mitochondrial morphology in wild-type (WT) or *Oma1*$^{-/-}$ BMDMs upon c-di-GMP, IFN-I, or CCCP treatment. The reduction in the mitochondrial footprint

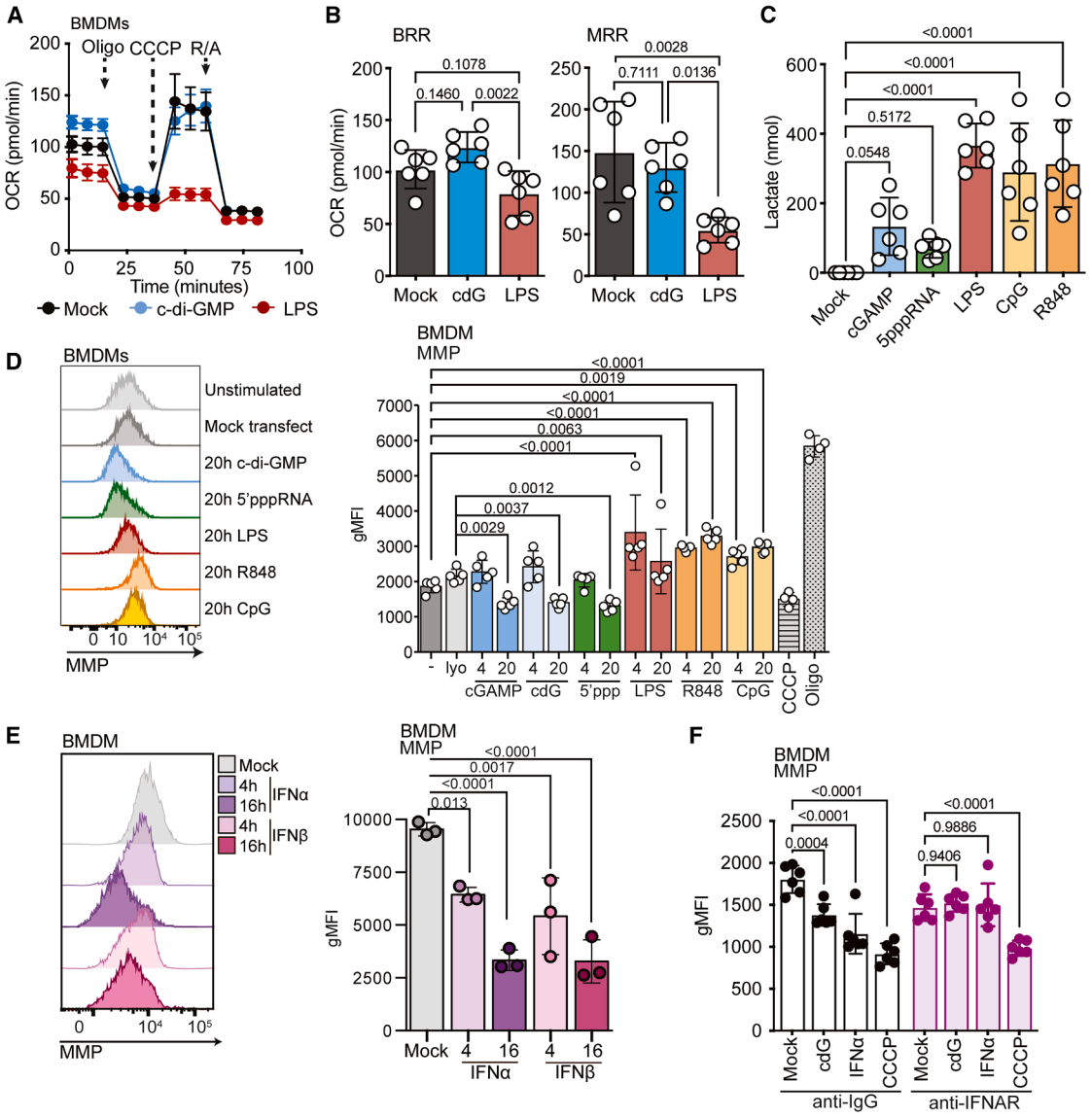

Figure 1. Cytosolic nucleic acid sensors induce an IFN-I-driven metabolic response

(A) Oxygen consumption rate (OCR) of BMDMs stimulated for 20 h with c-di-GMP (cdG), LPS, or mock-treated upon addition of oligomycin (Oligo), CCCP, and rotenone and antimycin A (R/A), $n = 6$, mean ± SEM.

(B) Basal respiratory rate (BRR, left) and maximal respiratory rate (MRR, right) in BMDMs treated as in (A), $n = 6$.

(C) Lactate quantification in supernatants from BMDMs treated as indicated for 24 h, $n = 6$.

(D) Representative histograms (left) and flow cytometric quantification of geometric mean fluorescence intensity values (geometric mean fluorescent intensity [gMFI], right) of TMRM staining in BMDMs stimulated as indicated. CCCP or oligomycin were used as controls, respectively. LyoVec (lyo), $n = 5$ (except CCCP and oligomycin conditions, $n = 4$).

(E) Representative histogram (left) and flow cytometric quantification of gMFI (right) of TMRM staining in BMDMs stimulated as indicated, $n = 3$.

(F) Flow cytometric quantification of TMRM gMFI in BMDMs pre-incubated with IFNAR-blocking antibody or isotype control before stimulation with cdG for 20 h, IFN-α for 4 h, or CCCP for 15 min, $n = 6$.

Data presented as mean ± SD except where indicated, representative of at least 2 independent experiments, except for (B), (C), and (F), which show a pool of 2 experiments. Analysis performed using one-way ANOVA with Tukey's multiple comparisons test (B and C), Dunnett's multiple comparisons test (D and E), and two-way ANOVA with Tukey's multiple comparisons test (F).

See also Figure S1.

and mean mitochondrial branch length following c-di-GMP and IFN-I treatment was OMA1 dependent (Figures 2C and S2B). However, the decrease in MMP upon stimulation was OMA1 independent (Figure 2D). MMP was also similarly decreased in WT and *Oma1*$^{-/-}$ peritoneal macrophages stimulated with c-di-GMP (Figure S2C). These results indicate that OMA1-dependent mitochondrial fission is downstream of the IFN-induced decrease in MMP and does not influence its induction.

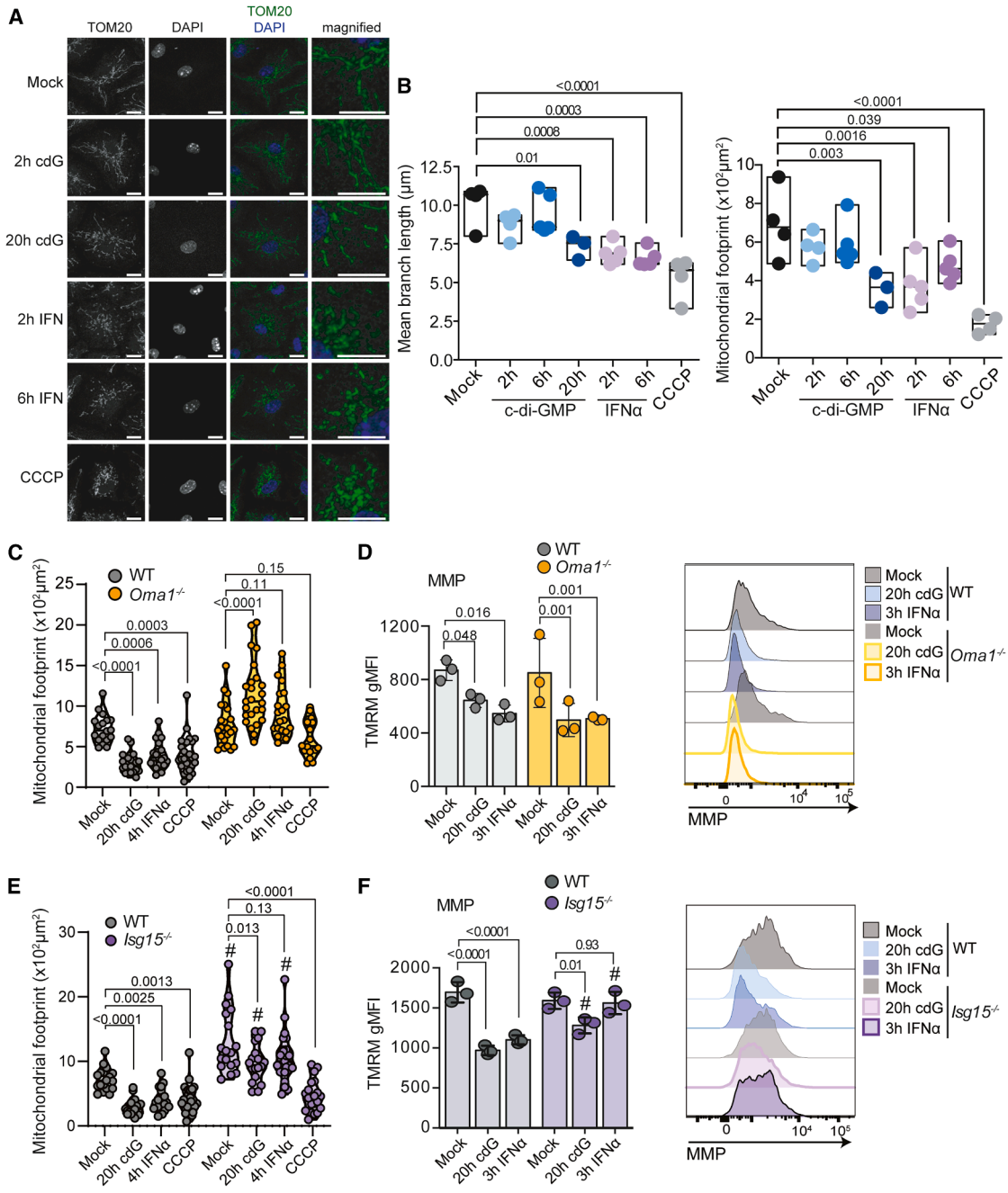

Figure 2. The ISG15-dependent drop in MMP occurs upstream of mitochondrial fission machinery

(A) Confocal microscopy of BMDMs stimulated as indicated. TOM20 (green), DAPI (blue); scale bar, 10 μm.

(B) Quantification of images as shown in (A). Each dot represents the average of at least 10 cells per field of view, $n = 3–5$.

(C) Quantification of mitochondrial footprint in WT and *Oma1*$^{-/-}$ BMDMs upon indicated treatments, $n = 3$ biological replicates; each point represents analysis of 1 cell, and at least 15 cells were analyzed per condition.

(D) Flow cytometric quantification of gMFI of TMRM (left) and representative histograms (right) in WT and *Oma1*$^{-/-}$ BMDMs stimulated with cdG for 20 h or IFN-α for 3 h, $n = 3$.

(E) Quantification of mitochondrial footprint in WT and ISG15-deficient BMDMs upon indicated treatments as performed in (B). # indicates significant differences between genotypes (mock $p < 0.0001$; 20 h cdG $p < 0.0001$; 4 h IFN-α $p < 0.0001$), $n = 3$ biological replicates; each point represents analysis of 1 cell, and at least 15 cells were analyzed per condition.

(F) Flow cytometric quantification of TMRM gMFI (left) and representative histograms (right) in WT and *Isg15*$^{-/-}$ BMDMs stimulated with cdG for 20 h or IFN-α for 3 h; # indicates significant differences between genotypes (20 h cdG $p = 0.026$; 3 h IFN-α $p = 0.0015$), $n = 3$.

(legend continued on next page)

IFN-I induces changes in target cells, mainly through ISG induction. One such ISG is ISG15, a 15-kDa ubiquitin-like molecule that can conjugate to target proteins, a process called ISGylation.[28] In the context of vaccinia virus (VACV) infection of macrophages, ISG15 was found to regulate mitochondrial function.[27] Based on this finding, we explored the role of ISG15 in direct IFN-I signaling in BMDMs. As expected, IFN-I treatment increased the *Isg15* mRNA expression in WT BMDMs (Figure S2D). Of note, *Isg15*$^{-/-}$ BMDMs displayed a higher mitochondrial footprint upon c-di-GMP or IFN-I treatment compared with WT BMDMs (Figure 2E). Moreover, the decrease in mitochondrial footprint and mean mitochondrial branch length observed in WT BMDMs upon IFN-I treatment was not observed in *Isg15*$^{-/-}$ BMDMs (Figures 2E and S2E). ISG15 deficiency prevented MMP loss upon IFN-I treatment, and the MMP of both c-di-GMP and IFN-I conditions in *Isg15*$^{-/-}$ cells was higher than that of their WT counterparts (Figure 2F). This effect was also observed in peritoneal macrophages from WT and *Isg15*$^{-/-}$ mice stimulated with IFN-I (Figure S2F). Both microscopy analysis and MMP staining showed that the effect of IFN-I was completely lost in *Isg15*$^{-/-}$ cells, whereas the effect of c-di-GMP was only partially lost, indicating additional IFN-independent pathways downstream of STING stimulation (Figures 2E, 2F, and S2E). These data indicate that IFN-I induces a decrease in MMP in an ISG15-dependent manner.

IFNAR signaling promotes ISGylation of mitochondrial proteins to increase ATP production and decrease MMP

Given the role of ISG15 in protein ISGylation, we hypothesized that ISG15 may function through conjugation to mitochondrial targets. Indeed, several proteomics studies have identified potential targets of ISGylation settings (Figure 3A).[41–44] Around 5% of reported ISGylated proteins were located in the mitochondria.[28] For comparison with published data, we immunoprecipitated ISG15 in WT and *Isg15*$^{-/-}$ BMDMs stimulated with IFN-β for 16 h. We identified several mitochondrial proteins that were co-immunoprecipitated with anti-ISG15 antibodies in WT but not in ISG15-deficient cells, including ATAD3, SLC25A5, and the ATP5B subunit of CV (Figure 3A; Table S1). We saw no effect on *Atp5f1b*, whether assessed by mRNA or protein expression in *Isg15*$^{-/-}$ cells (Figures S3A and S3B). We thus tested the effect of IFN-I treatment on CV activity by measuring ATP synthesis and found that IFN-β stimulation increased intracellular ATP in BMDMs (Figure 3B). ISG15 is first synthesized as a precursor that is cleaved to generate a carboxyl-terminal LRLRGG motif required for covalent attachment to target proteins—a process known as ISGylation.[45] To test whether ISGylation was required for its effect on ATP production and MMP, we tested the rescue of these impaired functions in ISG15-deficient BMDMs with an MVA-based vector expressing WT ISG15 (ISG15-GG) or a mutated form unable to perform ISGylation (ISG15-AA).[46] In terms of ATP production and MMP, the WT (ISG15-GG), but not the mutant (ISG15-AA), was able to recapitulate the WT response to IFN-I stimulation in *Isg15*$^{-/-}$ BMDMs (Figures 3C, 3D, and S3C), demonstrating that ISGylation activity is required for increased ATP production upon IFN-I stimulation. The increase in ATP production observed upon IFN-I treatment was OMA1 independent (Figure S3D), suggesting that it is a direct effect of ISG15 upstream of mitochondrial fission. These data indicate that the decrease in MMP in IFN-I-stimulated macrophages depends on ISGylation of target proteins and is associated with increased ATP production.

ISG15 is required for increased efferocytosis upon IFN-I stimulation

The analysis of *Oma1*$^{-/-}$ and *Isg15*$^{-/-}$ BMDMs upon IFN-I stimulation allowed the segregation of the primary ISG15-dependent effects, such as decreased MMP and increased ATP, from the subsequent ISG15- and OMA1-dependent increase in mitochondrial fission. We therefore investigated the contribution of both effects on macrophage function. A key role for macrophages is apoptotic cell (AC) uptake, or efferocytosis, to maintain tissue homeostasis.[47] MMP has been reported to inversely correlate with macrophage efferocytic capacity,[48] but the mechanism underlying this effect is not clear. We hypothesized that the reduced MMP observed upon IFN-I stimulation could increase efferocytosis and promote inflammation resolution. Following IFN-I treatment of BMDMs, we observed an increase in uptake of carboxyfluorescein succinimidyl ester (CFSE)-labeled ACs (Figure 4A). Confocal microscopy confirmed that stained ACs were internalized within macrophage actin cytoskeletons (Figure S4A). Both the number of efferocytic macrophages (Figure 4A) and the average efferocytic cargo per macrophage were increased (Figure S4B). Increasing doses of IFN-I did not further increase AC uptake, indicating a binary effect (Figure S4C). We then tested AC uptake upon IFN-I stimulation in WT BMDMs and BMDMs deficient in ISG15 or OMA1. *Isg15*$^{-/-}$ BMDMs showed no basal defect in efferocytosis but failed to increase AC uptake compared with WT macrophages upon IFN-I stimulation (Figure 4B). Conversely, OMA1 deficiency did not affect the increased efferocytosis observed upon IFN-I treatment (Figure 4B), suggesting that this effect is associated with the ISG15-dependent decrease in MMP and not with mitochondrial fission. We then tested the efferocytic capacity of peritoneal macrophages and observed the same pattern—IFN-I treatment increased AC uptake in WT and *Oma1*$^{-/-}$ macrophages but not in *Isg15*$^{-/-}$ macrophages (Figure 4C). There were no major changes in the expression of genes linked to efferocytic capacity in either *Isg15*$^{-/-}$ or *Oma1*$^{-/-}$ cells, except for an increased interleukin (IL)-10 induction in *Isg15*$^{-/-}$ cells (Figures S4D and S4E). These results indicate that ISG15 is required for the increase in efferocytosis observed in macrophages upon IFN-I stimulation.

To test the physiological relevance of IFN-I-induced efferocytosis, we focused on the thymus, a tissue with a high rate of efferocytosis. The thymus has constitutively high expression of

Data presented as mean ± SD (D and F), violin plots (C and E), or boxplots displaying the median and range (B), representative of at least 2 independent experiments. (C and E) Comparative analysis of WT vs. *Oma*1$^{-/-}$ and *Isg*15$^{-/-}$ BMDMs was done in the same set of experiments. For clarity, the analysis is shown separately in (C) and (E). Analysis performed using one-way ANOVA with Dunnett's multiple comparisons test (B), and two-way ANOVA with Tukey's multiple comparisons test (C–G).
See also Figure S2.

A

Dataset	ISGylated mitochondrial proteins
Our dataset (BMDMs + 16h IFNβ)	ATAD3, ATP5B, GLS, SLC25A5.
Zhang, et al., 2019 (Liver tissue + 72h Listeria infection)	ACAD11, ACO1, ACSL1, ACSL5, ALDH2, ASPDH, CAT, CLUH, CPT1A, CRAT, FASN, FBP1, FH, IDH1/3, IRGM1, MAT1A, MDH1, ME1, MTHFD1, NAMPT, NNMT, PC, SFXN1, SLC25A5, VDAC1/3
Peng et al., 2016 (A549 + influenza virus)	ATP5L
Wong et al., 2006 (A549 + 48h IFNβ)	ATP5F1A, ATP5F1B, CKMT1, FASN, MDH2, SLC25A5, SLC25A6
Zhao et al., 2005 (HeLa o/e ISG15 + 24h IFNβ)	ATP5A1, ATP5F1B, FARS2, FASN, OGDH, PHGDH

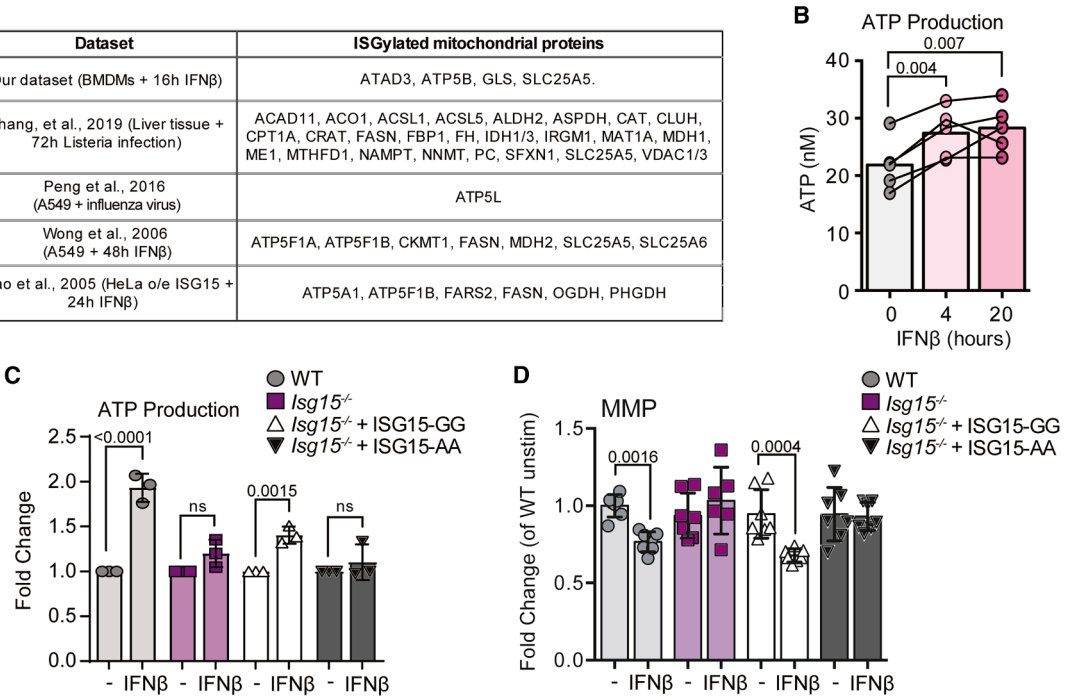

Figure 3. IFNAR signaling promotes ISGylation of mitochondrial proteins to increase ATP production and decrease MMP

(A) ISGylated mitochondrial proteins detected by proteomics upon 16 h of IFN-β treatment or in previously published datasets.

(B) Quantification of intracellular ATP in BMDMs treated with IFN-β for indicated times.

(C) Quantification of ATP in WT, *Isg15*$^{-/-}$, *Isg15*$^{-/-}$ + WT-ISG15 (ISG15-GG), or *Isg15*$^{-/-}$ + a conjugation mutant ISG15 (ISG15-AA) BMDMs stimulated with IFN-β for 4 h. The fold change compared with unstimulated cells is shown, $n = 5$.

(D) Flow cytometric quantification of TMRM gMFI in cells as in (C). Fold change compared with WT unstimulated is shown, $n = 3$.

Data presented as mean ± SD, representative of at least 2 independent experiments. Analysis performed using Repeated Measures one-way ANOVA with Tukey's multiple comparisons test (B) or two-way ANOVA with Šidak's multiple comparisons test (C and D).

See also Figure S3 and Table S1.

IFN-I,[49–51] resulting in increased ISG expression in thymic macrophages compared with other macrophage populations.[52] We hypothesized that increased IFN-I signaling may support the high phagocytic demand of the thymus compared with other organs. To test this, we injected WT, *Isg15*$^{-/-}$, and *Oma1*$^{-/-}$ mice with dexamethasone to augment thymocyte apoptosis, then quantified thymic cellularity (Figures 4D–4F). We observed decreased thymic cellularity in WT and *Oma1*$^{-/-}$ mice treated with dexamethasone compared with controls, compatible with massive thymocyte apoptosis and efficient efferocytosis. However, *Isg15*$^{-/-}$ mice did not show a significant decrease in thymic cellularity (Figures 4D–4F), suggesting impaired efferocytosis induction.[48] Indeed, active caspase-3^{+} cells were increased in *Isg15*$^{-/-}$ but not *Oma1*$^{-/-}$ thymi upon dexamethasone treatment compared with WT dexamethasone-treated thymi (Figure 4G), indicative of decreased efferocytosis in *Isg15*$^{-/-}$ mice. These experiments were performed in mice genetically ablated in all cells, and the effect observed could therefore depend on a contribution by non-hematopoietic cells, such as thymic epithelial cells. Because CD11b^{+} F4/80^{+} thymic macrophages can be reconstituted by bone marrow (BM) transplant,[53] we performed the same experiment in BM chimeras with WT control or *Isg15*$^{-/-}$ donors (Figure 4H). We found that, upon dexamethasone treatment, thymus size decreased less in mice reconstituted with *Isg15*$^{-/-}$ BM compared with WT-grafted control mice (Figure 4I). This was not due to differences in macrophage seeding of the thymus, as CD45.2^{+} reconstitution in the macrophage compartment was similar between both genotypes (Figure S4F). There was also an increase in active caspase-3^{+} cells in ISG15-deficient-reconstituted thymus compared with WT-reconstituted thymus controls (Figures 4J and S4G). Although pointing toward altered efferocytosis in *Isg15*$^{-/-}$ macrophages, these *in vivo* findings are indirect, measuring uncleared ACs in tissues. We therefore used an alternative assay of zymosan-induced peritonitis combined with the injection of labeled ACs into the peritoneum.[54,55] In the context of zymosan-induced peritonitis, peritoneal macrophages from *Isg15*$^{-/-}$ mice exhibited decreased uptake of ACs compared with their WT and *Oma1*$^{-/-}$ counterparts (Figures 4K and S4H). These data indicate that the ISG15-dependent regulation of macrophages upon IFN-I stimulation is important for dealing with increased efferocytic demand.

Efferocytosis is a highly regulated process that requires coordination of the actin cytoskeleton in order to phagocytose apoptotic cargo. This requires ATP-dependent F-actin polymerization.[56] Given our finding that IFN-I stimulation increased intracellular ATP in an ISG15-dependent manner, we hypothesized that this could affect the ratio of F-actin:G-actin. Indeed, IFN-I stimulation increased the F-actin:G-actin ratio, as observed by flow cytometry (Figure S4I). Notably, this increase in F-actin

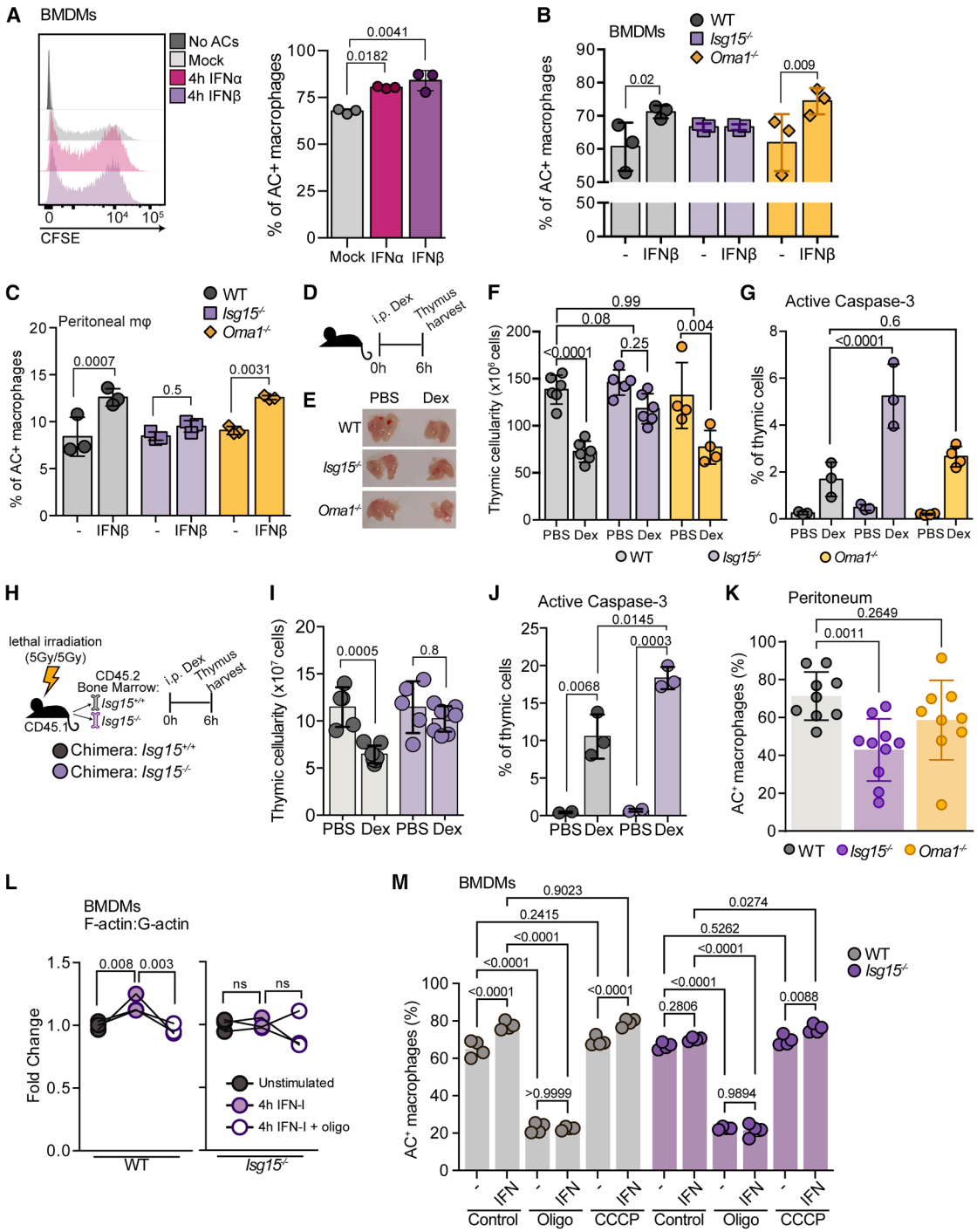

Figure 4. ISG15 is required for increased efferocytosis upon IFN-I stimulation

(A) Flow cytometric analysis of uptake of CFSE-labeled apoptotic cells (ACs) upon treatment of BMDMs with or without IFN-α or IFN-β for 4 h. Representative histograms (left) and quantification (right) are shown, $n = 3$.

(B) Percentage of CFSE$^+$ AC uptake in WT, *Isg15*$^{-/-}$, and *Oma1*$^{-/-}$ BMDMs stimulated with IFN-β or control for 4 h, $n = 3$.

(C) Flow cytometric analysis of CFSE$^+$ AC uptake in WT, *Isg15*$^{-/-}$, and *Oma1*$^{-/-}$ peritoneal macrophages stimulated with IFN-β or control for 4 h, $n = 3$.

(D) Schematic representation of thymic apoptosis induction.

(E) Representative images of thymi in WT, *Isg15*$^{-/-}$, and *Oma1*$^{-/-}$ mice treated as in (D).

(F) Quantification of total thymic cell numbers from mice treated as in (D), $n = 4–6$.

(G) Quantification of the percentage of cells expressing active caspase-3 in the thymi of mice treated as in (D), $n = 3–4$.

(H) Schematic of efferocytosis experiment in BM transplant mice.

(I) Thymic cellularity in *Isg15*$^{+/+}$ or *Isg15*$^{-/-}$ BM chimeric mice treated with dexamethasone for 4 h, $n = 5–7$.

(legend continued on next page)

polymerization did not occur in ISG15-deficient BMDMs and could be blocked in WT cells by inhibiting CV using oligomycin (Figure 4L). These findings result in two possible CV-driven mechanisms of increased IFN-I-induced efferocytosis: MMP depletion or increased ATP promoting F-actin polymerization. To test whether one or both mechanisms were responsible for the efferocytosis phenotype observed, we combined WT and *Isg15*$^{-/-}$ cell efferocytosis analysis with the inhibitors CCCP (decreasing MMP) or oligomycin (inhibiting CV activity). Although WT cells showed increased efferocytosis upon IFN-I stimulation, oligomycin prevented this effect and reduced basal efferocytic uptake, supporting the importance of CV activity in efferocytosis (Figure 4M). In *Isg15*$^{-/-}$ BMDMs, CCCP pre-treatment in combination with IFN-I rescued the IFN-induced increase in efferocytosis (Figure 4M). Together, these data support the conclusion that IFNAR stimulation promotes two CV-dependent processes—increased intracellular ATP and decreased MMP—and that forcing a decrease in MMP alone is sufficient to rescue the IFN-induced increase in efferocytosis in *Isg15*$^{-/-}$ macrophages.

IFN-induced mitochondrial fission negatively regulates ISG induction in macrophages

We then questioned whether OMA1 or ISG15 deficiency would affect other readouts of macrophage activation upon STING or IFNAR stimulation. We stimulated BMDMs with STING agonists and found no differences in *Ifnb* or *Il6* transcription in the absence of OMA1 or ISG15 (Figures S5A and S5B). Notably, stimulation of BMDMs with IFN-I resulted in increased ISG expression in the absence of OMA1, including *Ifit3* mRNA (Figure 5A) and Sca-1 (Ly6A/E)[57,58] (Figures 5B and S5C), indicating an enhanced feed-forward loop in the absence of OMA1. Given that OMA1 has other functions in the cell, independent of mitochondrial fission,[59,60] we tested the effect of Mdivi1, a mitochondrial fission inhibitor.[61] Pre-treatment of WT BMDMs with Mdivi1 also increased *Ifit3* mRNA along with Sca-1 expression upon IFN-I stimulation (Figures 5C, 5D, and S5D). A similar increase in ISG transcription and Sca-1 upregulation was also found in *Isg15*$^{-/-}$ BMDMs stimulated with IFN-I (Figures 5E, 5F, and S5E). These data point to ISG15- and OMA1-dependent mitochondrial fission as a negative regulator of downstream ISG induction upon IFN-I stimulation.

Given the importance of IFN-I in the control of viral replication, we tested the effect of ISG15 or OMA1 deficiency on VACV infection. Mice were infected with VACV in the ear pinnae (Figure 5G).[62] On days 2 and 7, ears were processed for analysis of viral titer. At day 2, we observed no differences in VACV titer in the ear between genotypes (Figure 5H). However, by day 7, both *Isg15*$^{-/-}$ and *Oma1*$^{-/-}$ mice showed decreased VACV titers compared with WT mice (Figure 5H). Further analysis of the immune compartment in the ear of these mice revealed a slight increase in monocytes and neutrophils in the ears of *Isg15*$^{-/-}$ mice upon infection (Figure S5F) and an increased frequency of late apoptotic neutrophils and monocytes (Figures S5G and S5H), in line with a potential defect in AC clearance. To exclude an effect in non-hematopoietic cells in the ear, we generated BM chimeras with WT, *Isg15*$^{-/-}$, or *Oma1*$^{-/-}$ donor BM (Figure 5I). In the chimera setting, mice with *Isg15*$^{-/-}$ or *Oma1*$^{-/-}$ BM showed decreased VACV titer in the ear on day 7 post infection (Figure 5J). These findings are in line with increased ISG induction in both *Isg15*$^{-/-}$ and *Oma1*$^{-/-}$ mice, supporting the physiological relevance of this effect, dependent on the hematopoietic cell compartment.

IFN-dependent mitochondrial fission decreases ER-mitochondria contacts to limit ISG induction

Mitochondrial fission decreases mitochondrial length and the length of contacts between mitochondria and neighboring organelles, such as the endoplasmic reticulum (ER).[63] Thus, we hypothesized that these contacts would be reduced upon IFN-I stimulation. The gold standard for ER-mitochondria detection is electron microscopy, which provides the resolution required to see these nanometer-scale contacts (i.e., regions of ER and mitochondria apposition narrower than 30 nm).[64] Using this technique, we observed a decrease in ER-mitochondria contacts upon IFN-I treatment (Figures 6A, 6B, and S6A). To confirm this decrease using an independent technique, we performed a fluorescence resonance energy transfer (FRET) experiment with fluorescent tethering partners targeted to the ER and the outer mitochondrial membrane, coupled to FRB and FKBP proteins, respectively, enabling their stabilization upon rapamycin supplementation.[64] FRB-FKBP heterodimerization only occurs when the organelles are naturally close, which can be detected by quantification of the FRET signal. Acute addition of rapamycin increased the FRET signal detected in transduced BMDMs, and this effect was decreased in BMDMs stimulated with c-di-GMP or IFN-α (Figure S6B). Thus, IFN-I-induced mitochondrial fission is also linked to decreased mitochondrial-ER communication.

We hypothesized that the decrease in ER-mitochondria contacts observed upon IFN-I treatment would not occur to the same extent in *Isg15*$^{-/-}$ and *Oma1*$^{-/-}$ BMDMs. Quantification of ER calnexin and mitochondrial TOM20 colocalization by confocal microscopy in BMDMs confirmed a decrease in ER-mitochondria proximity upon STING stimulation, which was dependent on IFNAR, as well as upon IFN-I treatment (Figures S6C and S6D). Notably, this decrease upon STING or IFNAR stimulation was lost in *Isg15*$^{-/-}$ BMDMs and dampened in *Oma1*$^{-/-}$ BMDMs (Figure 6C). ISG transcription is tightly controlled by phosphorylation and acetylation events.[65–67]

(J) Percentage of active caspase-3$^+$ cells in the thymus of *Isg15*$^{+/+}$ or *Isg15*$^{-/-}$ BM chimeric mice treated with dexamethasone for 4 h, $n = 3$.
(K) Percentage of F4/80$^+$CD11b$^+$CTV$^+$ cells in a model of zymosan-induced peritonitis in WT, *Isg15*$^{-/-}$, and *Oma1*$^{-/-}$ mice. A pool of 2 independent experiments is shown, $n = 9–10$.
(L) Flow cytometric analysis of the ratio of F-actin to G-actin gMFI in WT and *Isg15*$^{-/-}$ BMDMs stimulated with the indicated stimuli, $n = 3$.
(M) Percentage of CSFE$^+$ AC uptake in WT and *Isg15*$^{-/-}$ BMDMs treated as indicated with oligomycin or CCCP for 15 min prior to IFN-β or control for 4 h, $n = 4$.
Data presented as mean ± SD, representative of at least 2 independent experiments, except for (K), which is a pool of 2 independent experiments. Analysis performed using one-way ANOVA with Dunnett's multiple comparisons test (A and K), two-way ANOVA with Tukey's multiple comparisons test (B, C, F, G, I–K, and M), or paired *t* test (L).
See also Figure S4.

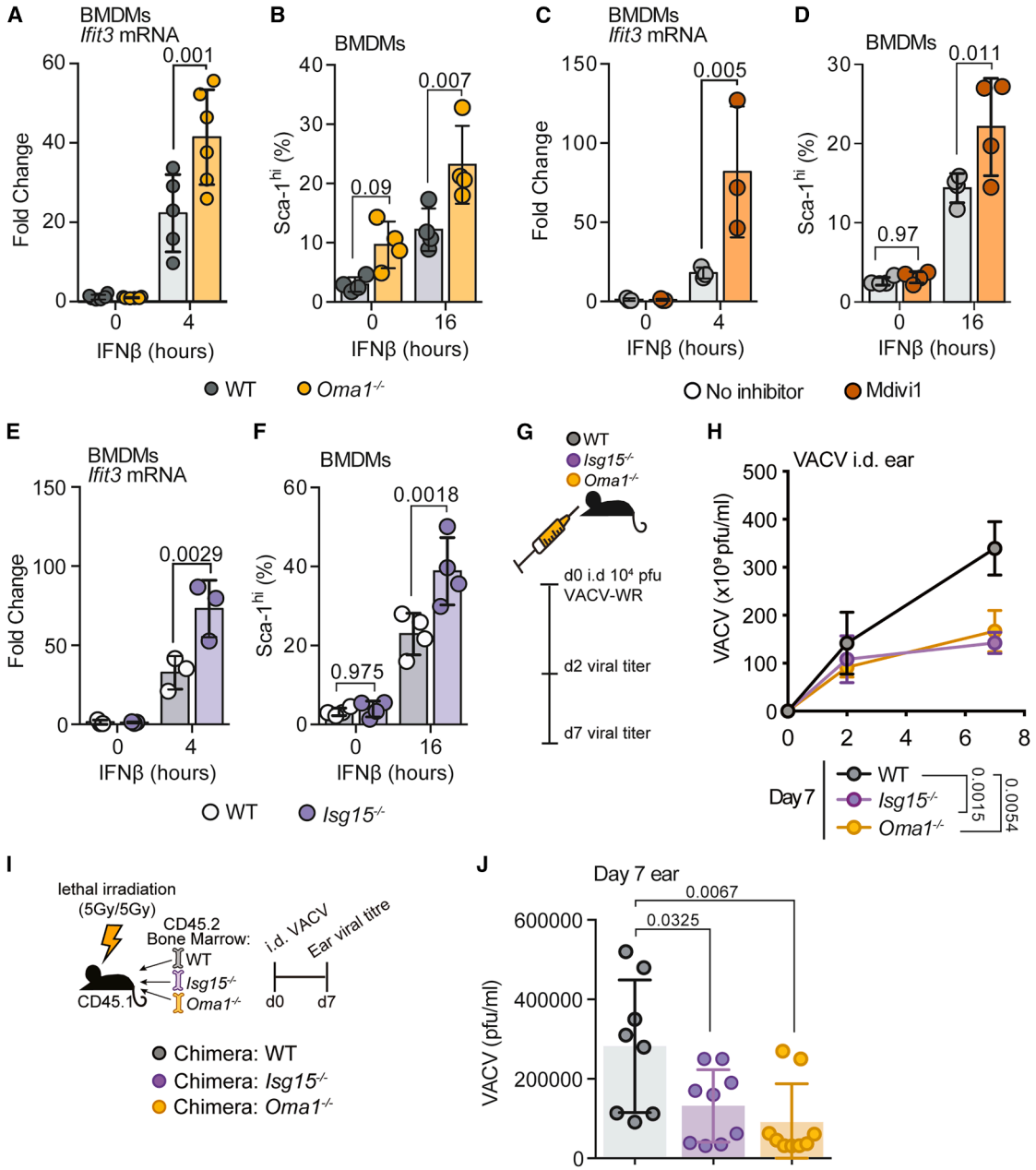

Figure 5. IFN-I-induced mitochondrial fission limits ISG induction in BMDMs

(A) *Ifit3* mRNA quantification in WT and *Oma1*$^{-/-}$ BMDMs treated with IFN-β for 0 or 4 h, n = 5–6.

(B) Flow cytometric analysis of Sca-1^{hi} cells in WT and *Oma1*$^{-/-}$ BMDMs treated or not with IFN-β for 16 h, n = 4.

(C) *Ifit3* mRNA quantification in WT BMDMs pre-treated or not with fission inhibitor Mdivi1 before IFN-β stimulation for 0 or 4 h, n = 3.

(D) Flow cytometric analysis of Sca-1^{hi} cells in WT BMDMs pre-treated or not with Mdivi1, then stimulated with IFN-β for 16 h, n = 4.

(E) *Ifit3* mRNA quantification in WT and *Isg15*$^{-/-}$ BMDMs treated with IFN-β for 0 or 4 h, n = 3.

(F) Flow cytometric quantification of Sca-1^{hi} cells in WT and *Isg15*$^{-/-}$ BMDMs treated or not with IFN-β for 16 h, n = 4.

(G) Schematic of VACV infection and experimental endpoints.

(H) VACV-infected and control ears from mice shown in (G) were processed for quantification of viral titer by plaque assay, n = 3–7, mean ± SEM.

(I) Experimental schematic of BM transplant, VACV infection, and experimental endpoint.

(J) Quantification of VACV viral titer in ears from mice shown in (I), n = 8–9.

Data presented as mean ± SD, except where indicated, representative of at least 2 independent experiments. (H) and (J) show a pool of 2 experiments. Analysis was performed using two-way ANOVA with Tukey's multiple comparisons test (A–F and H), and one-way ANOVA with Dunnett's multiple testing (J).

See also Figure S5.

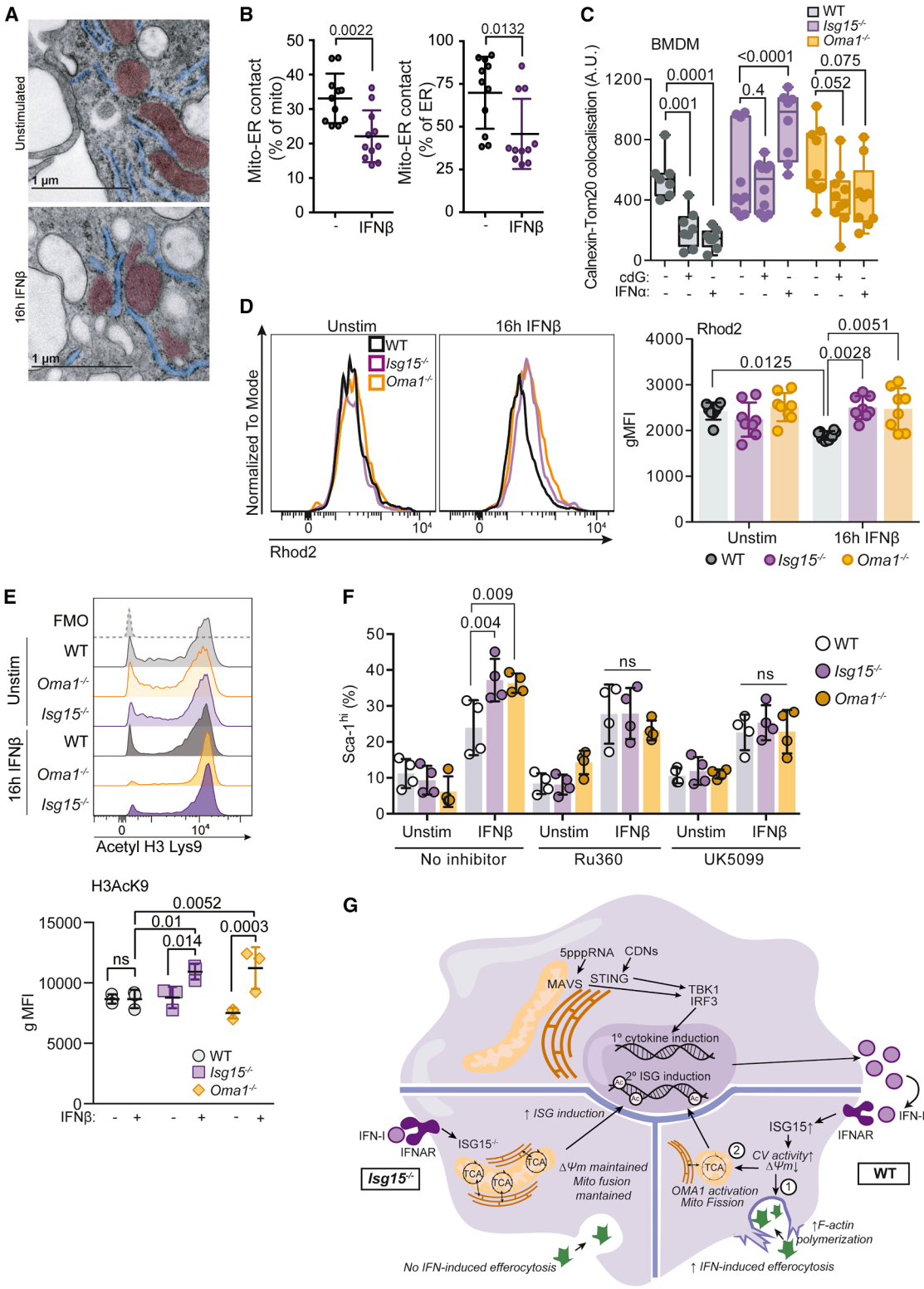

Figure 6. IFN-I-induced mitochondrial fission decreases ER-mitochondria contact sites and restrains ISG amplification

(A) Representative images from transmission electron microscopy of BMDMs stimulated with IFN-β for 0 or 16 h. Pseudocolor was added to images to show mitochondria (pink) and ER (blue).

(B) Quantification of the extension of ER-mitochondria (mito-ER) contacts, shown as a percentage of total mitochondria circumference (left) or total ER length (right), in cells treated as in (A); $n = 3$ with at least 10 sections analyzed per condition.

(legend continued on next page)

Both histone acetylation and deacetylation positively regulate IFNAR-dependent STAT activation and ISG transcription.[68–70] To examine the role of acetylation in IFNAR signaling in our setting, we supplemented cells with acetate to provide additional substrates for acetylation. In WT cells, acetate supplementation increased expression of the ISG Sca-1 upon IFN-I stimulation, supporting a positive role for acetylation in IFNAR-mediated regulation (Figures S6E and S6F).

We first hypothesized that sirtuins, a family of nicotinamide adenine dinucleotide (NAD)-dependent deacetylases reported to promote ISG transcription, could mediate changes in acetylation. However, we found only a slight increase in the NAD^+/nicotinamide adenine dinucleotide hydrogen (NADH) ratio in *Oma1*$^{-/-}$ BMDMs upon 16 h of IFN-I treatment, with no change in WT or *Isg15*$^{-/-}$ BMDMs (Figure S6G), suggesting that sirtuins are not the drivers of increased ISG induction in *Isg15*$^{-/-}$ and *Oma1*$^{-/-}$ BMDMs treated with IFN-I.

Given the role of ER contact sites in mitochondrial calcium regulation, we then tested mitochondrial calcium using the probe Rhod2. We observed no difference in unstimulated conditions in any genotype; however, upon IFN-β stimulation, there was a drop in mitochondrial calcium in WT BMDMs that was not observed in *Isg15*$^{-/-}$ and *Oma1*$^{-/-}$ BMDMs (Figure 6D). Mitochondrial calcium serves as a cofactor for several mitochondrial enzymes, including pyruvate dehydrogenase (PDH) phosphatase, a key enzyme in the regulation of tricarboxylic acid (TCA) cycle function and subsequent acetyl-coenzyme A (CoA) production.[71] We hypothesized that increased mitochondrial calcium availability could promote histone acetylation in the presence of signal-transducing transcription factors upon IFN-I stimulation, thereby increasing ISG production.[72] To test this, we measured acetylation of histone 3 lysine 9 (H3K9ac), a positive regulator of IFNAR signaling, by flow cytometry.[73] Both *Isg15*$^{-/-}$ and *Oma1*$^{-/-}$ BMDMs increased H3K9ac upon IFN-I stimulation compared with WT cells (Figure 6E).

To test the effect of ER-mitochondrial calcium regulation on ISG induction and histone acetylation upon IFNAR stimulation, we stimulated BMDMs with IFN-I in the presence or absence of an inhibitor of mitochondrial calcium uptake (Ru360) or an inhibitor of pyruvate entry into the TCA cycle (UK5099) in WT and *Isg15*$^{-/-}$ or *Oma1*$^{-/-}$ cells (Figure 6F). No difference was observed basally, yet upon IFN-I stimulation, both inhibitors prevented the increase in induction of Sca-1 in *Isg15*$^{-/-}$ and *Oma1*$^{-/-}$ BMDMs compared with WT BMDMs (Figure 6F). Therefore, the increase in ISG induction upon IFNAR stimulation in *Isg15*$^{-/-}$ and *Oma1*$^{-/-}$ BMDMs relied on mitochondrial calcium uptake and pyruvate entry into the TCA cycle. Pre-treatment with either compound also decreased the H3AcK9 detected in *Isg15*$^{-/-}$ BMDMs upon IFN-I stimulation (Figure S6H). Together, these data point to mitochondrial fission as a regulator of ER-mitochondria contact sites and mitochondrial calcium entry, regulating histone acetylation and IFNAR signaling (Figure 6G).

DISCUSSION

IFN-I is important for both initiation and resolution of inflammation.[30,74,75] Here, we have provided a mechanism by which IFN-I promotes the resolution of inflammation, boosting efferocytosis and restricting autocrine IFN-I signaling. The metabolic profile observed upon IFN-I treatment was characterized by low MMP and maintained mitochondrial oxygen consumption. Although low MMP is often associated with malfunctioning or damaged mitochondria, our results revealed that it may be associated with increased ATP synthesis. This resembles the behavior of low MMP T cells, which are more stem-like and show higher mitochondrial activity compared with their high-MMP counterparts.[76] However, a study in macrophages has shown a decrease in MMP associated with mitochondrial dysfunction during Mycobacteria infection associated with IFN-I,[77] while another study describes a link between low MMP and mtDNA release, activating cytosolic STING.[32] Therefore, although we observed an acute decrease in MMP alongside sustained OCR, this state may be transient and could result in mitochondrial dysfunction and DAMP release.

Based on the proteomics data that we and others have generated, we found that ISG15 conjugated to several mitochondrial targets, which could affect MMP.[28,41–44] In particular, ISG15 conjugated to subunits of mitochondrial CV, ATP synthase. CV ISGylation may increase ATP synthase activity and electron flow, thereby decreasing MMP. ISG15 can function independently of ISGylation[46]; however, we found that ISG15 conjugation to target proteins was essential for the reduced MMP and increased ATP production observed upon IFN-I. Other ISGylation targets include SCL25A5, an ADP/ATP translocase, which could also alter cellular ATP production.

Efferocytosis is an energy-demanding process, and sustained ATP production has previously been shown to be important for the uptake of efferocytic cargo.[56] However, ATP is just one factor in a highly regulated metabolism-dependent process. In IFN-I-stimulated macrophages, we find both increased cellular ATP concentrations and depleted MMP, the latter of which was previously found to be sufficient to increase efferocytic capacity.[48]

(C) Quantification of Tom20 and calnexin colocalization in confocal microscopy images of WT, *Oma1*$^{-/-}$, and *Isg15*$^{-/-}$ BMDMs stimulated with c-di-GMP for 0, 4, or 20 h. At least 10 cells per field of view were quantified. Each point indicates a biological replicate, $n = 7–10$.
(D) Representative histograms (left) and quantification of Rhod2 gMFI by flow cytometric analysis in WT, *Oma1*$^{-/-}$, and *Isg15*$^{-/-}$ BMDMs stimulated with or without IFN-β for 16 h, $n = 8$.
(E) Representative histograms (left) and flow cytometric quantification of acetylated lysine 9 residue on histone 3 (H3K9ac) gMFI (right) in WT, *Oma1*$^{-/-}$, and *Isg15*$^{-/-}$ BMDMs stimulated with IFN-β for 16 h, $n = 3$.
(F) Flow cytometric analysis of Sca-1^{hi} cells in WT, *Isg15*$^{-/-}$, and *Oma1*$^{-/-}$ BMDMs stimulated or not with IFN-β for 16 h in the presence or absence of UK5099 or Ru360, $n = 4$.
(G) Graphical summary of data presented.
Data presented as mean ± SD (B and D–F) or box and whiskers plot indicating median, quartiles, and range (C), representative of at least 2 independent experiments, except (C and D), which are a pool of 2 dent experiments. Analysis was performed using Student's *t* test (B) or two-way ANOVA with Tukey's multiple comparisons test (C–F).
See also Figure S6.

Our results using CCCP support the importance of MMP reduction in promoting efferocytosis. The downstream mechanism by which loss of MMP increases efferocytosis is unknown and will require further investigation.

A secondary consequence of MMP depletion is the induction of mitochondrial fission. Mitochondrial dynamics have previously been shown to promote continual efferocytosis.[78] However, in the context of IFN treatment, we saw no defect in the ability of *Oma1*$^{-/-}$ cells to efferocytose cargo. *In vivo*, both *Oma1*$^{-/-}$ and *Isg15*$^{-/-}$ mice showed enhanced control of VACV replication upon intradermal infection, indicating the physiological relevance of this ISG induction. It is important to note that other factors rather than direct IFNAR regulation can contribute to altered control of viral replication. It has been previously shown that ISG15 degrades USP18 and RIG-I to regulate IFN-I induction and RNA-induced responses, respectively.[79,80] ISG15 was also shown to directly ISGylate Drp1 to promote mitochondrial fission, indicating potential redundancy in this feedback loop.[81]

While increased IFN-I can be beneficial in viral infection, IFN-I should be tightly controlled to maintain organismal health. Excess production of IFN-I leads to systemic damage in interferopathies.[82] In the case of the thymus, high systemic concentrations of IFN-I and ISGs are found basally, promoting our hypothesis that this could support the high efferocytic demands of the organ. However, the thymus also requires cytokine regulation to avoid autoimmunity, such as in myasthenia gravis.[83]

ER-mitochondrial contacts are important for the transport of lipids and calcium to mitochondria, as well as for harboring several immune signaling proteins such as the nucleotide-binding domain, leucine-rich repeat, pyrin domain containing 3 (NLRP3) inflammasome.[84] A recent study in T cells has shown that more ER-mitochondrial contacts correlate with increased cytokine production, dependent on mitochondrial calcium transport.[85] In the context of ISG induction, it is known that the IFN-β enhanceosome depends on the recruitment of histone acetyltransferases to acetylate the nucleosome, resulting in chromatin remodeling.[66] Our results, showing increased H3K9ac upon IFN-I treatment in the absence of ISG15 or OMA1, support the importance of acetylation for autocrine IFN-I signaling[67] and the notion that ER-mitochondrial contacts support increased TCA cycle activity and, subsequently, enhanced ISG transcription.

In conclusion, we propose that IFNAR induction of ISG15 is linked to ISGylation of mitochondrial proteins, leading to an increase in intracellular ATP and a loss of MMP, associated with increased efferocytic capacity. This decreased MMP also activates OMA1 and mitochondrial fission in BMDMs, reducing ER-mitochondrial contacts and negatively regulating histone acetylation and ISG induction. Given the promise of IFN-I in clinical settings such as cancer, but its current lack of success,[86] an increased understanding of metabolic adaptations downstream of IFNAR may help explain the multifunctional roles of this cytokine.

Limitations of the study

We have shown the role of ISGylation in MMP and ATP production and identified proteins of mitochondrial CV as candidate targets; other ISGylated targets may be important in this response, both inside and outside of the mitochondria.[28] Although we demonstrated that IFN-I treatment correlates with changes in mitochondrial morphology, we did not directly measure activation of the fission machinery. Mechanistically, the decrease in MMP upon IFN-I stimulation was found to enhance efferocytosis, consistent with previous findings on uncoupling protein 2 (UCP2).[48] Because MMP influences numerous intracellular processes, the pathway by which it regulates efferocytosis remains unclear. *In vivo* studies were performed using mice with a genetic deletion of *Isg15* or *Oma1*, as well as ablated or chimeric mice with hematopoietic-specific deletion; however, we cannot exclude the possibility that this signaling axis acts on non-macrophage cell types. Another open question is whether altered efferocytosis affects subsequent cytokine induction, as was shown for IL-10 production in post-efferocytic macrophages.[87] It remains to be studied what threshold of IFN-I signaling triggers this response *in vivo* and how tonic IFN-I signaling shapes these effects. Further studies are required to determine the metabolic and epigenetic states of cells with increased mitochondrial fusion upon IFN-I treatment to elucidate the underlying mechanisms.

RESOURCE AVAILABILITY

Lead contact

Requests for further information and resources should be directed to, and will be fulfilled by, the lead contact, David Sancho (dsancho@cnic.es).

Materials availability

This study did not generate new unique reagents.

Data and code availability

All data are available in the main text or the supplemental information.

ACKNOWLEDGMENTS

We thank the D.S. laboratory for scientific discussions and Professor Jesús Vázquez and Dr. Enrique Calvo of the CNIC Proteomics Service for their expertise.

The D.S. laboratory received support from the CNIC; the Ministerio de Ciencia, Innovación y Universidades (MICIU) (PID2022-137712OB-I00, CPP2021-008310, CPP2022-009762, and CPP2024-011365); MICIU/AEI/10.13039/501100011033 Agencia Estatal de Investigación, Unión Europea NextGenerationEU/PRTR; Comunidad de Madrid (P2022/BMD-7333 INMUNOVAR-CM); the Scientific Foundation of the Spanish Association Against Cancer (AECC-PRYGN246642SANC); Worldwide Cancer Research (WWCR-25-0080); Fundación CRIS contra el cáncer (excellence2025_03); the European Union (ERC-2023-PoC GA-101158245-ImnovAth); and the "La Caixa" Foundation (LCF/PR/HR23/52430012 and LCF/PR/HR22/52420019). M.A.d.P. acknowledges support from the Spanish Ministry of Science, Innovation & Universities (MICIU)/Agencia Estatal de Investigación (AEI)/FEDER (PID2023-146414OB-I00/AEI/10.13039/501100011033); from ERDF/EU; and from the Comunidad de Madrid (TecNanoBio-CM, ref. TEC-2024/TEC-158). This project has received funding from the European Union's Horizon 2020 research and innovation programme under the Marie Skłodowska-Curie grant agreement no. 892965. G.D. is supported by a European Molecular Biology Organization Long-term Fellowship ALTF 379-2019. I.A.-B. is supported by a Beca de Formación del Profesorado Universitario (FPU) fellowship (FPU18/05752). I.H.-M. is supported by a La Caixa INPhINIT fellowship (ID 100010434, fellowship code: LCF/BQ/IN17/11620074). E.M.-R. is a recipient of support from the Comunidad Autonoma de Madrid (PIPF-2023/SAL-GL-29932). A.J.-C. is supported by a Beca de Formación del Profesorado Universitario (FPU) fellowship (FPU18/05434). M.S.-A. is supported by the MICIU (RYC2020-029690-I and PID2021-128106NA-I00). Flow cytometry was conducted at the CNIC Flow Cytometry Unit. Microscopy was conducted at Microscopy & Dynamic Imaging, CNIC. The CNIC is supported by the Instituto de Salud Carlos III (ISCIII),

the MICIU, and the Pro CNIC Foundation, and is a Severo Ochoa Center of Excellence (CEX2020-001041-S funded by MICIU/AEI /10.13039/501100011033).

AUTHOR CONTRIBUTIONS

Conceptualization, G.D. and D.S.; methodology, G.D., I.F.-D., C.V.-B., M.S.-A., M.A.d.P., S.G., and D.S.; investigation, G.D., I.A.-B., I.F.-D., C.V.-B., A.J.-C., I.H.-M., and M.S.-A.; funding acquisition, G.D. and D.S.; supervision, G.D. and D.S.; writing – original draft, G.D. and D.S.; writing – review and editing, G.D., D.S., I.A.-B., I.F.-D., C.V.-B., I.H.-M., E.M.-R., M.S.-A., M.A.d.P., A.J.-C., S.G., and F.S.-M.

DECLARATION OF INTERESTS

The authors declare no competing interests.

STAR★METHODS

Detailed methods are provided in the online version of this paper and include the following:

- KEY RESOURCES TABLE
- METHOD DETAILS
  - Mice
  - Cell culture
  - Visualization of ER-mitochondrial contact by FRET measurements
  - Efferocytosis Assays
  - Bone marrow graft
  - Zymosan-induced peritonitis
  - Viral Infection and Quantification
  - Flow cytometry
  - Confocal microscopy
  - Extracellular Flux Assay
  - Analysis of supernatant
  - Transmission electron microscopy
  - Quantitative Real-time PCR
  - Western Blot
  - Proteomics
  - Statistical analysis

SUPPLEMENTAL INFORMATION

Supplemental information can be found online at https://doi.org/10.1016/j.immuni.2025.12.010.

Received: February 11, 2025
Revised: October 28, 2025
Accepted: December 15, 2025
Published: January 28, 2026

REFERENCES

1. Wculek, S.K., Dunphy, G., Heras-Murillo, I., Mastrangelo, A., and Sancho, D. (2022). Metabolism of tissue macrophages in homeostasis and pathology. Cell. Mol. Immunol. *19*, 384–408. https://doi.org/10.1038/s41423-021-00791-9.
2. Brubaker, S.W., Bonham, K.S., Zanoni, I., and Kagan, J.C. (2015). Innate Immune Pattern Recognition: A Cell Biological Perspective. Annu. Rev. Immunol. *33*, 257–290. https://doi.org/10.1146/annurev-immunol-032414-112240.
3. Ostuni, R., Piccolo, V., Barozzi, I., Polletti, S., Termanini, A., Bonifacio, S., Curina, A., Prosperini, E., Ghisletti, S., and Natoli, G. (2013). Latent Enhancers Activated by Stimulation in Differentiated Cells. Cell *152*, 157–171. https://doi.org/10.1016/j.cell.2012.12.018.
4. Everts, B., Amiel, E., Huang, S.C.C., Smith, A.M., Chang, C.H., Lam, W.Y., Redmann, V., Freitas, T.C., Blagih, J., Van Der Windt, G.J.W., et al. (2014). TLR-driven early glycolytic reprogramming via the kinases TBK1-IKKε supports the anabolic demands of dendritic cell activation. Nat. Immunol. *15*, 323–332. https://doi.org/10.1038/ni.2833.
5. Bailis, W., Shyer, J.A., Zhao, J., Canaveras, J.C.G., Al Khazal, F.J., Qu, R., Steach, H.R., Bielecki, P., Khan, O., Jackson, R., et al. (2019). Distinct modes of mitochondrial metabolism uncouple T cell differentiation and function. Nature *571*, 403–407. https://doi.org/10.1038/s41586-019-1311-3.
6. Mills, E.L., Kelly, B., Logan, A., Costa, A.S.H., Varma, M., Bryant, C.E., Tourlomousis, P., Däbritz, J.H.M., Gottlieb, E., Latorre, I., et al. (2016). Succinate Dehydrogenase Supports Metabolic Repurposing of Mitochondria to Drive Inflammatory Macrophages. Cell *167*, 457–470.e13. https://doi.org/10.1016/j.cell.2016.08.064.
7. Lampropoulou, V., Sergushichev, A., Bambouskova, M., Nair, S., Vincent, E.E., Loginicheva, E., Cervantes-Barragan, L., Ma, X., Huang, S.C.C., Griss, T., et al. (2016). Itaconate Links Inhibition of Succinate Dehydrogenase with Macrophage Metabolic Remodeling and Regulation of Inflammation. Cell Metab. *24*, 158–166. https://doi.org/10.1016/j.cmet.2016.06.004.
8. West, A.P., Brodsky, I.E., Rahner, C., Woo, D.K., Erdjument-Bromage, H., Tempst, P., Walsh, M.C., Choi, Y., Shadel, G.S., and Ghosh, S. (2011). TLR signalling augments macrophage bactericidal activity through mitochondrial ROS. Nature *472*, 476–480. https://doi.org/10.1038/nature09973.
9. Everts, B., Amiel, E., van der Windt, G.J.W., Freitas, T.C., Chott, R., Yarasheski, K.E., Pearce, E.L., and Pearce, E.J. (2012). Commitment to glycolysis sustains survival of NO-producing inflammatory dendritic cells. Blood *120*, 1422–1431. https://doi.org/10.1182/blood-2012-03-419747.
10. Guak, H., Al Habyan, S., Ma, E.H., Aldossary, H., Al-Masri, M., Won, S.Y., Ying, T., Fixman, E.D., Jones, R.G., McCaffrey, L.M., et al. (2018). Glycolytic metabolism is essential for CCR7 oligomerization and dendritic cell migration. Nat. Commun. *9*, 2463. https://doi.org/10.1038/s41467-018-04804-6.
11. Michelucci, A., Cordes, T., Ghelfi, J., Pailot, A., Reiling, N., Goldmann, O., Binz, T., Wegner, A., Tallam, A., Rausell, A., et al. (2013). Immune-responsive gene 1 protein links metabolism to immunity by catalyzing itaconic acid production. Proc. Natl. Acad. Sci. USA *110*, 7820–7825. https://doi.org/10.1073/pnas.1218599110.
12. Lachmandas, E., Boutens, L., Ratter, J.M., Hijmans, A., Hooiveld, G.J., Joosten, L.A.B., Rodenburg, R.J., Fransen, J.A.M., Houtkooper, R.H., Van Crevel, R., et al. (2016). Microbial stimulation of different Toll-like receptor signalling pathways induces diverse metabolic programmes in human monocytes. Nat. Microbiol. *2*, 16246. https://doi.org/10.1038/nmicrobiol.2016.246.
13. Tannahill, G.M., Curtis, A.M., Adamik, J., Palsson-Mcdermott, E.M., McGettrick, A.F., Goel, G., Frezza, C., Bernard, N.J., Kelly, B., Foley, N.H., et al. (2013). Succinate is an inflammatory signal that induces IL-1β through HIF-1α. Nature *496*, 238–242. https://doi.org/10.1038/nature11986.
14. Vila, I.K., Chamma, H., Steer, A., Saccas, M., Taffoni, C., Turtoi, E., Reinert, L.S., Hussain, S., Marines, J., Jin, L., et al. (2022). STING orchestrates the crosstalk between polyunsaturated fatty acid metabolism and inflammatory responses. Cell Metab. *34*, 125–139.e8. https://doi.org/10.1016/j.cmet.2021.12.007.
15. Decout, A., Katz, J.D., Venkatraman, S., and Ablasser, A. (2021). The cGAS–STING pathway as a therapeutic target in inflammatory diseases. Nat. Rev. Immunol. *21*, 548–569. https://doi.org/10.1038/s41577-021-00524-z.
16. Sun, L., Wu, J., Du, F., Chen, X., and Chen, Z.J. (2013). Cyclic GMP-AMP synthase is a cytosolic DNA sensor that activates the type I interferon pathway. Science *339*, 786–791. https://doi.org/10.1126/science.1232458.
17. Ablasser, A., Goldeck, M., Cavlar, T., Deimling, T., Witte, G., Röhl, I., Hopfner, K.P., Ludwig, J., and Hornung, V. (2013). CGAS produces a 2′-5′-linked cyclic dinucleotide second messenger that activates STING. Nature *498*, 380–384. https://doi.org/10.1038/nature12306.

18. Ishikawa, H., and Barber, G.N. (2008). STING is an endoplasmic reticulum adaptor that facilitates innate immune signalling. Nature *455*, 674–678. https://doi.org/10.1038/nature07317.

19. Lima-Junior, D.S., Krishnamurthy, S.R., Bouladoux, N., Collins, N., Han, S.-J., Chen, E.Y., Constantinides, M.G., Link, V.M., Lim, A.I., Enamorado, M., et al. (2021). Endogenous retroviruses promote homeostatic and inflammatory responses to the microbiota. Cell *184*, 3794–3811.e19. https://doi.org/10.1016/j.cell.2021.05.020.

20. Schaupp, L., Muth, S., Rogell, L., Kofoed-Branzk, M., Melchior, F., Lienenklaus, S., Ganal-Vonarburg, S.C., Klein, M., Guendel, F., Hain, T., et al. (2020). Microbiota-Induced Type I Interferons Instruct a Poised Basal State of Dendritic Cells. Cell *181*, 1080–1096.e19. https://doi.org/10.1016/j.cell.2020.04.022.

21. Duong, E., Fessenden, T.B., Lutz, E., Dinter, T., Yim, L., Blatt, S., Bhutkar, A., Wittrup, K.D., and Spranger, S. (2021). Type I interferon activates MHC class I-dressed CD11b+ conventional dendritic cells to promote protective anti-tumor CD8+ T cell immunity. Immunity *55*, 308–323.e9. https://doi.org/10.1016/j.immuni.2021.10.020.

22. De Giovanni, M., Cutillo, V., Giladi, A., Sala, E., Maganuco, C.G., Medaglia, C., Di Lucia, P., Bono, E., Cristofani, C., Consolo, E., et al. (2020). Spatiotemporal regulation of type I interferon expression determines the antiviral polarization of CD4+ T cells. Nat. Immunol. *21*, 321–330. https://doi.org/10.1038/s41590-020-0596-6.

23. Wu, D., Sanin, D.E., Everts, B., Chen, Q., Qiu, J., Buck, M.D., Patterson, A., Smith, A.M., Chang, C.H., Liu, Z., et al. (2016). Type 1 Interferons Induce Changes in Core Metabolism that Are Critical for Immune Function. Immunity *44*, 1325–1336. https://doi.org/10.1016/j.immuni.2016.06.006.

24. Gautier, G., Humbert, M., Deauvieau, F., Scuiller, M., Hiscott, J., Bates, E.E.M., Trinchieri, G., Caux, C., and Garrone, P. (2005). A type I interferon autocrine–paracrine loop is involved in Toll-like receptor-induced interleukin-12p70 secretion by dendritic cells. J. Exp. Med. *201*, 1435–1446. https://doi.org/10.1084/jem.20041964.

25. Ivashkiv, L.B., and Donlin, L.T. (2014). Regulation of type I interferon responses. Nat. Rev. Immunol. *14*, 36–49. https://doi.org/10.1038/nri3581.

26. Perng, Y.-C., and Lenschow, D.J. (2018). ISG15 in antiviral immunity and beyond. Nat. Rev. Microbiol. *16*, 423–439. https://doi.org/10.1038/s41579-018-0020-5.

27. Baldanta, S., Fernández-Escobar, M., Acín-Perez, R., Albert, M., Camafeita, E., Jorge, I., Vázquez, J., Enríquez, J.A., and Guerra, S. (2017). ISG15 governs mitochondrial function in macrophages following vaccinia virus infection. PLoS Pathog. *13*, e1006651. https://doi.org/10.1371/journal.ppat.1006651.

28. Albert, M., Bécares, M., Falqui, M., Fernández-Lozano, C., and Guerra, S. (2018). ISG15, a Small Molecule with Huge Implications: Regulation of Mitochondrial Homeostasis. Viruses *10*, 629. https://doi.org/10.3390/v10110629.

29. Channappanavar, R., Fehr, A.R., Zheng, J., Wohlford-Lenane, C., Abrahante, J.E., Mack, M., Sompallae, R., McCray, P.B., Meyerholz, D.K., and Perlman, S. (2019). IFN-I response timing relative to virus replication determines MERS coronavirus infection outcomes. J. Clin. Investig. *129*, 3625–3639. https://doi.org/10.1172/JCI126363.

30. Kumaran Satyanarayanan, S., El Kebir, D., Soboh, S., Butenko, S., Sekheri, M., Saadi, J., Peled, N., Assi, S., Othman, A., Schif-Zuck, S., et al. (2019). IFN-β is a macrophage-derived effector cytokine facilitating the resolution of bacterial inflammation. Nat. Commun. *10*, 3471. https://doi.org/10.1038/s41467-019-10903-9.

31. Murphy, M.P. (2009). How mitochondria produce reactive oxygen species. Biochem. J. *417*, 1–13. https://doi.org/10.1042/BJ20081386.

32. Mertens, R.T., Misra, A., Xiao, P., Baek, S., Rone, J.M., Mangani, D., Sivanathan, K.N., Arojojoye, A.S., Awuah, S.G., Lee, I., et al. (2024). A metabolic switch orchestrated by IL-18 and the cyclic dinucleotide cGAMP programs intestinal tolerance. Immunity *57*, 2077–2094.e12. https://doi.org/10.1016/j.immuni.2024.06.001.

33. Sanin, D.E., Matsushita, M., Klein Geltink, R.I., Grzes, K.M., van Teijlingen Bakker, N., Corrado, M., Kabat, A.M., Buck, M.D., Qiu, J., Lawless, S.J., et al. (2018). Mitochondrial Membrane Potential Regulates Nuclear Gene Expression in Macrophages Exposed to Prostaglandin E2. Immunity *49*, 1021–1033.e6. https://doi.org/10.1016/j.immuni.2018.10.011.

34. Keating, S.E., Baran, M., and Bowie, A.G. (2011). Cytosolic DNA sensors regulating type I interferon induction. Trends Immunol. *32*, 574–581. https://doi.org/10.1016/j.it.2011.08.004.

35. Pantel, A., Teixeira, A., Haddad, E., Wood, E.G., Steinman, R.M., and Longhi, M.P. (2014). Direct Type I IFN but Not MDA5/TLR3 Activation of Dendritic Cells Is Required for Maturation and Metabolic Shift to Glycolysis after Poly IC Stimulation. PLoS Biol. *12*, e1001759. https://doi.org/10.1371/journal.pbio.1001759.

36. Zhang, K., Li, H., and Song, Z. (2014). Membrane depolarization activates the mitochondrial protease OMA1 by stimulating self-cleavage. EMBO Rep. *15*, 576–585. https://doi.org/10.1002/embr.201338240.

37. Gilkerson, R., De La Torre, P., and St Vallier, S. (2021). Mitochondrial OMA1 and OPA1 as Gatekeepers of Organellar Structure/Function and Cellular Stress Response. Front. Cell Dev. Biol. *9*, 626117. https://doi.org/10.3389/fcell.2021.626117.

38. Valente, A.J., Maddalena, L.A., Robb, E.L., Moradi, F., and Stuart, J.A. (2017). A simple ImageJ macro tool for analyzing mitochondrial network morphology in mammalian cell culture. Acta Histochem. *119*, 315–326. https://doi.org/10.1016/j.acthis.2017.03.001.

39. Li, Y., He, Y., Miao, K., Zheng, Y., Deng, C., and Liu, T.-M. (2020). Imaging of macrophage mitochondria dynamics in vivo reveals cellular activation phenotype for diagnosis. Theranostics *10*, 2897–2917. https://doi.org/10.7150/thno.40495.

40. Neikirk, K., Lopez, E.-G., Marshall, A.G., Alghanem, A., Krystofiak, E., Kula, B., Smith, N., Shao, J., Katti, P., and Hinton, A. (2023). Call to action to properly utilize electron microscopy to measure organelles to monitor disease. Eur. J. Cell Biol. *102*, 151365. https://doi.org/10.1016/j.ejcb.2023.151365.

41. Zhang, Y., Thery, F., Wu, N.C., Luhmann, E.K., Dussurget, O., Foecke, M., Bredow, C., Jiménez-Fernández, D., Leandro, K., Beling, A., et al. (2019). The in vivo ISGylome links ISG15 to metabolic pathways and autophagy upon Listeria monocytogenes infection. Nat. Commun. *10*, 5383. https://doi.org/10.1038/s41467-019-13393-x.

42. Peng, Q.-S., Li, G.-P., Sun, W.-C., Yang, J.-B., Quan, G.-H., and Liu, N. (2016). Analysis of ISG15-Modified Proteins from A549 Cells in Response to Influenza Virus Infection by Liquid Chromatography-Tandem Mass Spectrometry. Chin. J. Anal. Chem. *44*, 850–856. https://doi.org/10.1016/S1872-2040(16)60936-2.

43. Wong, J.J.Y., Pung, Y.F., Sze, N.S.-K., and Chin, K.-C. (2006). HERC5 is an IFN-induced HECT-type E3 protein ligase that mediates type I IFN-induced ISGylation of protein targets. Proc. Natl. Acad. Sci. USA *103*, 10735–10740. https://doi.org/10.1073/pnas.0600397103.

44. Zhao, C., Denison, C., Huibregtse, J.M., Gygi, S., and Krug, R.M. (2005). Human ISG15 conjugation targets both IFN-induced and constitutively expressed proteins functioning in diverse cellular pathways. Proc. Natl. Acad. Sci. USA *102*, 10200–10205. https://doi.org/10.1073/pnas.0504754102.

45. Narasimhan, J., Potter, J.L., and Haas, A.L. (1996). Conjugation of the 15-kDa Interferon-induced Ubiquitin Homolog Is Distinct from That of Ubiquitin. J. Biol. Chem. *271*, 324–330. https://doi.org/10.1074/jbc.271.1.324.

46. Falqui, M., Perdiguero, B., Coloma, R., Albert, M., Marcos-Villar, L., McGrail, J.P., Sorzano, C.Ó.S., Esteban, M., Gómez, C.E., and Guerra, S. (2023). An MVA-based vector expressing cell-free ISG15 increases IFN-I production and improves HIV-1-specific CD8 T cell immune responses. Front. Cell. Infect. Microbiol. *13*, 1187193. https://doi.org/10.3389/fcimb.2023.1187193.

47. Morioka, S., Maueröder, C., and Ravichandran, K.S. (2019). Living on the Edge: Efferocytosis at the Interface of Homeostasis and Pathology. Immunity *50*, 1149–1162. https://doi.org/10.1016/j.immuni.2019.04.018.

48. Park, D., Han, C.Z., Elliott, M.R., Kinchen, J.M., Trampont, P.C., Das, S., Collins, S., Lysiak, J.J., Hoehn, K.L., and Ravichandran, K.S. (2011).

Continued clearance of apoptotic cells critically depends on the phagocyte Ucp2 protein. Nature *477*, 220–224. https://doi.org/10.1038/nature10340.

49. Otero, D.C., Baker, D.P., and David, M. (2013). IRF7-dependent IFN-β production in response to RANKL promotes medullary thymic epithelial cell development. J. Immunol. *190*, 3289–3298. https://doi.org/10.4049/jimmunol.1203086.

50. Colantonio, A.D., Epeldegui, M., Jesiak, M., Jachimowski, L., Blom, B., and Uittenbogaart, C.H. (2011). IFN-α Is Constitutively Expressed in the Human Thymus, but Not in Peripheral Lymphoid Organs. PLoS One *6*, e24252. https://doi.org/10.1371/journal.pone.0024252.

51. Lienenklaus, S., Cornitescu, M., Ziętara, N., Łyszkiewicz, M., Gekara, N., Jabłońska, J., Edenhofer, F., Rajewsky, K., Bruder, D., Hafner, M., et al. (2009). Novel Reporter Mouse Reveals Constitutive and Inflammatory Expression of IFN-β In Vivo. J. Immunol. *183*, 3229–3236. https://doi.org/10.4049/jimmunol.0804277.

52. Zhou, T.-A., Hsu, H.-P., Tu, Y.-H., Cheng, H.-K., Lin, C.-Y., Chen, N.-J., Tsai, J.-W., Robey, E.A., Huang, H.-C., Hsu, C.-L., et al. (2022). Thymic macrophages consist of two populations with distinct localization and origin. eLife *11*, e75148. https://doi.org/10.7554/eLife.75148.

53. Tacke, R., Hilgendorf, I., Garner, H., Waterborg, C., Park, K., Nowyhed, H., Hanna, R.N., Wu, R., Swirski, F.K., Geissmann, F., et al. (2015). The transcription factor NR4A1 is essential for the development of a novel macrophage subset in the thymus. Sci. Rep. *5*, 10055. https://doi.org/10.1038/srep10055.

54. Newson, J., Stables, M., Karra, E., Arce-Vargas, F., Quezada, S., Motwani, M., Mack, M., Yona, S., Audzevich, T., and Gilroy, D.W. (2014). Resolution of acute inflammation bridges the gap between innate and adaptive immunity. Blood *124*, 1748–1764. https://doi.org/10.1182/blood-2014-03-562710.

55. Proto, J.D., Doran, A.C., Gusarova, G., Yurdagul, A., Sozen, E., Subramanian, M., Islam, M.N., Rymond, C.C., Du, J., Hook, J., et al. (2018). Regulatory T Cells Promote Macrophage Efferocytosis during Inflammation Resolution. Immunity *49*, 666–677.e6. https://doi.org/10.1016/j.immuni.2018.07.015.

56. Merlin, J., Ivanov, S., Dumont, A., Sergushichev, A., Gall, J., Stunault, M., Ayrault, M., Vaillant, N., Castiglione, A., Swain, A., et al. (2021). Non-canonical glutamine transamination sustains efferocytosis by coupling redox buffering to oxidative phosphorylation. Nat. Metab. *3*, 1313–1326. https://doi.org/10.1038/s42255-021-00471-y.

57. Dumont, F.J., and Coker, L.Z. (1986). Interferon-α/β enhances the expression of Ly-6 antigens on T cells *in vivo* and *in vitro*. Eur. J. Immunol. *16*, 735–740. https://doi.org/10.1002/eji.1830160704.

58. Essers, M.A.G., Offner, S., Blanco-Bose, W.E., Waibler, Z., Kalinke, U., Duchosal, M.A., and Trumpp, A. (2009). IFNα activates dormant haematopoietic stem cells in vivo. Nature *458*, 904–908. https://doi.org/10.1038/nature07815.

59. Guo, X., Aviles, G., Liu, Y., Tian, R., Unger, B.A., Lin, Y.T., Wiita, A.P., Xu, K., Correia, M.A., and Kampmann, M. (2020). Mitochondrial stress is relayed to the cytosol by an OMA1–DELE1–HRI pathway. Nature *579*, 427–432. https://doi.org/10.1038/s41586-020-2078-2.

60. Fessler, E., Eckl, E.M., Schmitt, S., Mancilla, I.A., Meyer-Bender, M.F., Hanf, M., Philippou-Massier, J., Krebs, S., Zischka, H., and Jae, L.T. (2020). A pathway coordinated by DELE1 relays mitochondrial stress to the cytosol. Nature *579*, 433–437. https://doi.org/10.1038/s41586-020-2076-4.

61. Cassidy-Stone, A., Chipuk, J.E., Ingerman, E., Song, C., Yoo, C., Kuwana, T., Kurth, M.J., Shaw, J.T., Hinshaw, J.E., Green, D.R., et al. (2008). Chemical Inhibition of the Mitochondrial Division Dynamin Reveals Its Role in Bax/Bak-Dependent Mitochondrial Outer Membrane Permeabilization. Dev. Cell *14*, 193–204. https://doi.org/10.1016/j.devcel.2007.11.019.

62. Tscharke, D.C., and Smith, G.L. (1999). A model for vaccinia virus pathogenesis and immunity based on intradermal injection of mouse ear pinnae. J. Gen. Virol. *80*, 2751–2755. https://doi.org/10.1099/0022-1317-80-10-2751.

63. Szabadkai, G., Simoni, A.M., Chami, M., Wieckowski, M.R., Youle, R.J., and Rizzuto, R. (2004). Drp-1-Dependent Division of the Mitochondrial Network Blocks Intraorganellar Ca2+ Waves and Protects against Ca2+-Mediated Apoptosis. Mol. Cell *16*, 59–68. https://doi.org/10.1016/j.molcel.2004.09.026.

64. Csordás, G., Várnai, P., Golenár, T., Roy, S., Purkins, G., Schneider, T.G., Balla, T., and Hajnóczky, G. (2010). Imaging Interorganelle Contacts and Local Calcium Dynamics at the ER-Mitochondrial Interface. Mol. Cell *39*, 121–132. https://doi.org/10.1016/j.molcel.2010.06.029.

65. Honda, K., Yanai, H., Negishi, H., Asagiri, M., Sato, M., Mizutani, T., Shimada, N., Ohba, Y., Takaoka, A., Yoshida, N., et al. (2005). IRF-7 is the master regulator of type-I interferon-dependent immune responses. Nature *434*, 772–777. https://doi.org/10.1038/nature03464.

66. Agalioti, T., Lomvardas, S., Parekh, B., Yie, J., Maniatis, T., and Thanos, D. (2000). Ordered Recruitment of Chromatin Modifying and General Transcription Factors to the IFN-β Promoter. Cell *103*, 667–678. https://doi.org/10.1016/S0092-8674(00)00169-0.

67. Tang, X., Gao, J.-S., Guan, Y.J., McLane, K.E., Yuan, Z.-L., Ramratnam, B., and Chin, Y.E. (2007). Acetylation-Dependent Signal Transduction for Type I Interferon Receptor. Cell *131*, 93–105. https://doi.org/10.1016/j.cell.2007.07.034.

68. Krämer, O.H., Knauer, S.K., Greiner, G., Jandt, E., Reichardt, S., Gührs, K.-H., Stauber, R.H., Böhmer, F.D., and Heinzel, T. (2009). A phosphorylation-acetylation switch regulates STAT1 signaling. Genes Dev. *23*, 223–235. https://doi.org/10.1101/gad.479209.

69. Kosciuczuk, E.M., Mehrotra, S., Saleiro, D., Kroczynska, B., Majchrzak-Kita, B., Lisowski, P., Driehaus, C., Rogalska, A., Turner, A., Lienhoop, T., et al. (2019). Sirtuin 2–mediated deacetylation of cyclin-dependent kinase 9 promotes STAT1 signaling in type I interferon responses. J. Biol. Chem. *294*, 827–837. https://doi.org/10.1074/jbc.RA118.005956.

70. Paulson, M., Press, C., Smith, E., Tanese, N., and Levy, D.E. (2002). IFN-Stimulated transcription through a TBP-free acetyltransferase complex escapes viral shutoff. Nat. Cell Biol. *4*, 140–147. https://doi.org/10.1038/ncb747.

71. Rizzuto, R., De Stefani, D., Raffaello, A., and Mammucari, C. (2012). Mitochondria as sensors and regulators of calcium signalling. Nat. Rev. Mol. Cell Biol. *13*, 566–578. https://doi.org/10.1038/nrm3412.

72. Suomalainen, A., and Nunnari, J. (2024). Mitochondria at the crossroads of health and disease. Cell *187*, 2601–2627. https://doi.org/10.1016/j.cell.2024.04.037.

73. Génin, P., Lin, R., Hiscott, J., and Civas, A. (2012). Recruitment of Histone Deacetylase 3 to the Interferon-A Gene Promoters Attenuates Interferon Expression. PLoS One *7*, e38336. https://doi.org/10.1371/journal.pone.0038336.

74. Gough, D.J., Messina, N.L., Clarke, C.J.P., Johnstone, R.W., and Levy, D.E. (2012). Constitutive Type I Interferon Modulates Homeostatic Balance through Tonic Signaling. Immunity *36*, 166–174. https://doi.org/10.1016/j.immuni.2012.01.011.

75. Hervas-Stubbs, S., Perez-Gracia, J.L., Rouzaut, A., Sanmamed, M.F., Le Bon, A., and Melero, I. (2011). Direct effects of type I interferons on cells of the immune system. Clin. Cancer Res. *17*, 2619–2627. https://doi.org/10.1158/1078-0432.CCR-10-1114.

76. Sukumar, M., Liu, J., Mehta, G.U., Patel, S.J., Roychoudhuri, R., Crompton, J.G., Klebanoff, C.A., Ji, Y., Li, P., Yu, Z., et al. (2016). Mitochondrial Membrane Potential Identifies Cells with Enhanced Stemness for Cellular Therapy. Cell Metab. *23*, 63–76. https://doi.org/10.1016/j.cmet.2015.11.002.

77. Olson, G.S., Murray, T.A., Jahn, A.N., Mai, D., Diercks, A.H., Gold, E.S., and Aderem, A. (2021). Type I interferon decreases macrophage energy metabolism during mycobacterial infection. Cell Rep. *35*, 109195. https://doi.org/10.1016/j.celrep.2021.109195.

78. Wang, Y., Subramanian, M., Yurdagul, A., Barbosa-Lorenzi, V.C., Cai, B., de Juan-Sanz, J., Ryan, T.A., Nomura, M., Maxfield, F.R., and Tabas, I. (2017). Mitochondrial Fission Promotes the Continued Clearance of Apoptotic Cells by Macrophages. Cell *171*, 331–345.e22. https://doi.org/10.1016/j.cell.2017.08.041.

79. Kim, M.-J., Hwang, S.-Y., Imaizumi, T., and Yoo, J.-Y. (2008). Negative Feedback Regulation of RIG-I-Mediated Antiviral Signaling by Interferon-Induced ISG15 Conjugation. J. Virol. *82*, 1474–1483. https://doi.org/10.1128/JVI.01650-07.

80. Zhang, X., Bogunovic, D., Payelle-Brogard, B., Francois-Newton, V., Speer, S.D., Yuan, C., Volpi, S., Li, Z., Sanal, O., Mansouri, D., et al. (2015). Human intracellular ISG15 prevents interferon-α/β over-amplification and auto-inflammation. Nature *517*, 89–93. https://doi.org/10.1038/nature13801.

81. Das, P., and Chakrabarti, O. (2024). ISGylation of DRP1 closely balances other post-translational modifications to mediate mitochondrial fission. Cell Death Dis. *15*, 184. https://doi.org/10.1038/s41419-024-06543-7.

82. Crow, Y.J., and Stetson, D.B. (2022). The type I interferonopathies: 10 years on. Nat. Rev. Immunol. *22*, 471–483. https://doi.org/10.1038/s41577-021-00633-9.

83. Cufi, P., Dragin, N., Ruhlmann, N., Weiss, J.M., Fadel, E., Serraf, A., Berrih-Aknin, S., and Le Panse, R. (2014). Central role of interferon-beta in thymic events leading to myasthenia gravis. J. Autoimmun. *52*, 44–52. https://doi.org/10.1016/j.jaut.2013.12.016.

84. Hayashi, T., Rizzuto, R., Hajnoczky, G., and Su, T.P. (2009). MAM: more than just a housekeeper. Trends Cell Biol. *19*, 81–88. https://doi.org/10.1016/j.tcb.2008.12.002.

85. Yang, J.-F., Xing, X., Luo, L., Zhou, X.-W., Feng, J.-X., Huang, K.-B., Liu, H., Jin, S., Liu, Y.-N., Zhang, S.-H., et al. (2023). Mitochondria-ER contact mediated by MFN2-SERCA2 interaction supports $CD8^+$ T cell metabolic fitness and function in tumors. Sci. Immunol. *8*, eabq2424. https://doi.org/10.1126/sciimmunol.abq2424.

86. Zhang, X., Wang, S., Zhu, Y., Zhang, M., Zhao, Y., Yan, Z., Wang, Q., and Li, X. (2021). Double-edged effects of interferons on the regulation of cancer-immunity cycle. OncoImmunology *10*, 1929005. https://doi.org/10.1080/2162402X.2021.1929005.

87. Zhang, S., Weinberg, S., DeBerge, M., Gainullina, A., Schipma, M., Kinchen, J.M., Ben-Sahra, I., Gius, D.R., Yvan-Charvet, L., Chandel, N.S., et al. (2019). Efferocytosis Fuels Requirements of Fatty Acid Oxidation and the Electron Transport Chain to Polarize Macrophages for Tissue Repair. Cell Metab. *29*, 443–456.e5. https://doi.org/10.1016/j.cmet.2018.12.004.

88. Latorre-Pellicer, A., Lechuga-Vieco, A.V., Johnston, I.G., Hämäläinen, R.H., Pellico, J., Justo-Méndez, R., Fernández-Toro, J.M., Clavería, C., Guaras, A., Sierra, R., et al. (2019). Regulation of Mother-to-Offspring Transmission of mtDNA Heteroplasmy. Cell Metab. *30*, 1120–1130.e5. https://doi.org/10.1016/j.cmet.2019.09.007.

89. Quirós, P.M., Ramsay, A.J., Sala, D., Fernández-Vizarra, E., Rodríguez, F., Peinado, J.R., Fernández-García, M.S., Vega, J.A., Enríquez, J.A., Zorzano, A., et al. (2012). Loss of mitochondrial protease OMA1 alters processing of the GTPase OPA1 and causes obesity and defective thermogenesis in mice. EMBO J. *31*, 2117–2133. https://doi.org/10.1038/emboj.2012.70.

90. Osiak, A., Utermöhlen, O., Niendorf, S., Horak, I., and Knobeloch, K.-P. (2005). ISG15, an Interferon-Stimulated Ubiquitin-Like Protein, Is Not Essential for STAT1 Signaling and Responses against Vesicular Stomatitis and Lymphocytic Choriomeningitis Virus. Mol. Cell. Biol. *25*, 6338–6345. https://doi.org/10.1128/mcb.25.15.6338-6345.2005.

91. Schindelin, J., Arganda-Carreras, I., Frise, E., Kaynig, V., Longair, M., Pietzsch, T., Preibisch, S., Rueden, C., Saalfeld, S., Schmid, B., et al. (2012). Fiji: an open-source platform for biological-image analysis. Nat. Methods *9*, 676–682. https://doi.org/10.1038/nmeth.2019.

92. Iborra, S., Izquierdo, H.M., Martínez-López, M., Blanco-Menéndez, N., Reis e Sousa, C., and Sancho, D. (2012). The DC receptor DNGR-1 mediates cross-priming of CTLs during vaccinia virus infection in mice. J. Clin. Invest. *122*, 1628–1643. https://doi.org/10.1172/JCI60660.

93. Keller, A., Nesvizhskii, A.I., Kolker, E., and Aebersold, R. (2002). Empirical Statistical Model To Estimate the Accuracy of Peptide Identifications Made by MS/MS and Database Search. Anal. Chem. *74*, 5383–5392. https://doi.org/10.1021/ac025747h.

94. Nesvizhskii, A.I., Keller, A., Kolker, E., and Aebersold, R. (2003). A Statistical Model for Identifying Proteins by Tandem Mass Spectrometry. Anal. Chem. *75*, 4646–4658. https://doi.org/10.1021/ac0341261.

STAR★METHODS

KEY RESOURCES TABLE

REAGENT or RESOURCE	SOURCE	IDENTIFIER
Antibodies		
Anti-mouse CD16/CD32 (clone 2.4G2)	Tonbo Biosciences	Cat# 70-0161; RRID: AB_2621487
Anti-mouse F4/80 Monoclonal Antibody (clone BM8), PE, eBioscience™	Thermo Fisher Scientific	Cat#12-4801-82; RRID: AB_465923
CD11b Monoclonal Antibody (M1/70), eFluor 660, eBioscience™	Thermo Fisher Scientific	Cat#50-0112-80; RRID: AB_11218677
InVivoMAb anti-mouse IFNAR-1 (clone MAR1-5A3)	BioXCell	Cat#BE0241; RRID: AB_2687723
Anti-mouse Tom20 Antibody (clone FL-145)	Santa Cruz Biotechnology	Cat#sc-11415; RRID: AB_2207533
Anti-mouse Calnexin (AF18)	Santa Cruz Biotechnology	Cat#sc-23954; RRID: AB_626783
CD45.1 Monoclonal Antibody (A20), APC, eBioscience™	Thermo Fisher Scientific	Cat# 17-0453-82; RRID: AB_469398
APC/Fire™ 750 anti-mouse CD45.1 Antibody	Biolegend	Cat#110752; RRID: AB_2629806
BD Horizon™ V450 Mouse Anti-Mouse CD45.2 (clone 104)	BD Biosciences	Cat#560697; RRID: AB_1727495
CD45 Monoclonal Antibody (30-F11), APC-eFluor™ 780, eBioscience™	Thermo Fisher Scientific	Cat#47-0451-82; RRID: AB_1548781
MHC Class II (I-A/I-E) Monoclonal Antibody (M5/114.15.2), APC-eFluor 780, eBioscience™	Thermo Fisher Scientific	Cat# 47-5321-80; RRID: AB_1548783
BD Pharmingen™ PerCP-Cy™5.5 Rat Anti-Mouse I-A/I-E Clone M5/114.15.2 (RUO)	BD Pharmingen™	Cat# 562363; RRID: AB_11153297
Brilliant Violet 421™ anti-mouse CD64	Biolegend	Cat#139309; RRID: AB_2562694
BV786 Rat Anti-Mouse CD90.2 Clone 30-H12	BD Biosciences	Cat#740841; RRID: AB_2740495
BD Pharmingen™ FITC Rat Anti-Mouse Ly-6C Clone AL-21 (RUO)	BD Biosciences	Cat#561085; RRID: AB_394628
Ly-6C Monoclonal Antibody (HK1.4), PerCP-Cyanine5.5, eBioscience™	Thermo Fisher Scientific	Cat#45-5932-82;RRID:AB_2723343
BD Pharmingen™ PE Rat Anti-Mouse Ly-6G Clone 1A8 (RUO)	BD Biosciences	Cat#551461; RRID: AB_394208
Anti-ISG15 (Clone F-9)	Santa Cruz Biotechnology	Cat#sc-166755; RRID: AB_2126308
Mouse Anti-Mitochondrial ATP Synthase Subunit Beta Monoclonal Antibody, Unconjugated, Clone 3D5	Abcam	Cat# ab14730; RRID: AB_301438
Acetyl-Histone H3 (Lys9) (C5B11) Rabbit mAb	Cell Signaling	Cat#9649; RRID: AB_823528
Ly-6A/E (Sca-1) Monoclonal Antibody (D7), PE-Cyanine7, eBioscience™	Invitrogen	Cat#25-5981-82; RRID: AB_469669
Goat anti-Mouse IgG (H+L) Cross-Adsorbed Secondary Antibody, Alexa Fluor™ 488	Thermo Fisher Scientific	Cat#A-11001; RRID:AB_2534069
Goat anti-Rabbit IgG (H+L) Highly Cross-Adsorbed Secondary Antibody, Alexa Fluor™ 647	Thermo Fisher Scientific	Cat#A-21245; RRID:AB_2535813
Bacterial and virus strains		
Vaccinia virus Western Reserve (VACV-WR)	Jonathan W. Yewdell and Jack R. Bennink (NIH, Bethesda, Maryland, USA)	N/A

(*Continued on next page*)

Continued

REAGENT or RESOURCE	SOURCE	IDENTIFIER
MVA-Δ3-ISG15 virus (AA or GG)	Falqui et al.[46]	DOI: 10.3389/fcimb.2023.1187193
Chemicals, peptides, and recombinant proteins		
Liberase™ TL Research Grade	Sigma-Aldrich	Cat#5401020001
DNase I, Bovine Pancreas, > 2000U/MG	Biomatik	Cat#A4193
DAPI (4',6-Diamidino-2-Phenylindole, Dihydrochloride)	Thermo Fisher Scientific	Cat#D1306; RRID: AB_2629482
Ghost Dye™ Red 780	TonboBIO	Cat# 13-0865-T500
Hoechst 33342	Thermo Fischer Scientific	Cat# H3570
Red Blood Cell Lysing Buffer Hybri-Max™	Sigma-Aldrich	Cat#R7757
Oligomycin	Sigma-Aldrich	Cat#O4876
Carbonyl Cyanide 3-chlorophenylhydrazone (CCCP)	Sigma-Aldrich	Cat#C2759
Rotenone	Sigma-Aldrich	Cat#R8875
Antimycin A	Sigma-Aldrich	Cat#A8674
Tetramethylrhodamine methyl ester perchlorate (TMRM)	Sigma-Aldrich	Cat#T5428
JC-1	Enzo Lifesciences	Cat#ENZ-52304
Mouse IFN Beta, Mammalian	PBL assay science	Cat#12405-1
Recombinant Mouse IFN-alpha 2/IFNA2	R&D Systems	Cat#10149-IF-010
Lyophilized cationic lipid for transfection of mammalian cells	Invivogen	Cat#lyec-2
2'3' GAMP	Biolog	Cat#C161
c-di-GMP	Biolog	Cat# C057-05
5' triphosphate double stranded RNA	Invivogen	Cat#tlrl-3prna
LPS-EK	Invivogen	Cat# tlrl-eklps
R848	Invivogen	Cat#tlrl-r848-5
CpG ODN 1826	Invivogen	Cat# tlrl-1826-1
Zymosan	Invivogen	Cat# tlrl-zyn
Phalloidin-Alexa Fluor 647	Invitrogen	Cat#A22287
Deoxyribonuclease I, Alexa Fluor™ 488 Conjugate	Invitrogen	Cat#D12371
Mdivi-1	Sigma	Cat#M0199
UK-5099 inhibitor of Mitochondrial Pyruvate Carrier	MedChem Express	Cat#HY-15475
Ru360 inhibitor of mitochondrial Ca2+ uptake	Sigma Aldrich	Cat#557440
SIRT-IN-1	MedChem Express	Cat#HY-16615
Rapamycin Ready Made Solution, 2.5 mg/mL in DMSO (2.74 mM)	Sigma Aldrich	Cat#R8781
Rhod-2 AM (Bromide)	StemCell Technologies	Cat#100-0994
H2DCFDA	Thermo Fisher	Cat#D399
MitoTEMPO	Sigma Aldrich	Cat# SML0737
CellTrace™ Violet	Invitrogen	Cat# C34557
CellTrace™ CFSE Cell Proliferation Kit	Invitrogen	Cat# C34554
Dexamethasone	Sigma	Cat#D4902
Crystal Violet	Sigma	Cat#C0775
RPMI Medium 1640	Gibco	Cat#11875093
Paraformaldehyde (PFA) 16% (w/v)	Thermo Fisher	Cat# 28908
Triton X-100	Sigma Aldrich	Cat#X100
Mouse anti-rabbit IgG PE-Cy7	Santa Cruz Biotechnology	Cat#sc-516721
Immobilon Forte Western HRP Substrate	Millipore	Cat#638179

(*Continued on next page*)

Continued

REAGENT or RESOURCE	SOURCE	IDENTIFIER
Critical commercial assays		
NAD/NADH-Glo™ Assay	Promega	Cat#G9071
LumiKine Xpress mIFN-β 2.0	Invivogen	Cat#luex-mifnbv2
R&D Systems™ Mouse CCL5/RANTES DuoSet ELISA	Fisher Scientific	Cat#30021809
Luminescent ATP Detection Assay Kit	Abcam	Cat#ab113849
FITC Active Caspase-3 Apoptosis Kit	BD Pharmigen	Cat#550480
Lactate assay kit	Merck	Cat#MAK064-1KT
Pierce™ BCA Protein Assay Kit	Thermo Fisher Scientific	Cat#23225
RNeasy Micro Kit	QIAGEN	Cat# 74004
QIAamp DNA Mini Kit	QIAGEN	Cat# 51304
High-Capacity cDNA Reverse Transcription Kit	Applied Biosystems	Cat#4368814
GoTaq qPCR Master Mix	Promega	Cat#A6001
Seahorse XFe96 FluxPak	Agilent	Cat#103792-100
FITC Annexin V Apoptosis Detection Kit with PI	Biolegend	Cat#640914
Experimental models: Cell lines		
Immortalized Mouse Embryonic Fibroblasts (MEFs)	Latorre-Pellicer et al.[88]	doi: 10.1016/j.cmet.2019.09.007
CV1	ATCC CCL-70	N/A
Experimental models: Organisms/strains		
OMA1$^{-/-}$ mice	Quirós et al.[89]	doi: 10.1038/emboj.2012.70
ISG15$^{-/-}$ mice	Osiak et al.[90]	DOI: 10.1128/MCB.25.14.6338-6345.2005; PMID: 15988020
Oligonucleotides		
Primers for qRT-PCR, see Table S2	This study	N/A
Recombinant DNA		
pLVX- [OMM-FKBP-YFP]-P2A-[CFP- FRB-ER] (FEMP lentivirally delivered probe)	This study	N/A
Software and algorithms		
ImageJ/Fiji	Schindelin et al.[91]	https://imagej.net/software/fiji/
GraphPad Prism version 9	GraphPad Software	https://www.graphpad.com
BD FACSDiva™ Software	BD Biosciences	https://www.bdbiosciences.com/
FlowJo v10	Tree Star	https://www.flowjo.com/
SDS software version 2.4 (Applied Biosystems 7900HT Fast Real-Time PCR System Software)	Thermo Fisher Scientific	https://www.thermofisher.com/
Seahorse Wave Desktop Software	Agilent technologies	https://www.agilent.com
Other		
ProLong™ Gold Antifade Mounting media	Life Technologies	Cat#P36930

METHOD DETAILS

Mice

Male and female C57BL/6 CD45.2 WT, CD45.1 WT, *Oma1*$^{-/-}$, and *Isg15*$^{-/-}$ mice maintained on chow diet were used between 8 and 12 weeks of age for all experiments. The local ethics committee approved all animal studies (PROEX 026/17 and PROEX 115/19), and all animal procedures were compliant with the EU Directive 2010/63/EU and Recommendation 2007/526/EC regarding the protection of animals used for experimental and other scientific purposes, enforced by the Spanish law under RD 1201/2005.

Cell culture

Cells were routinely cultured in R10 media (RPMI (Gibco) supplemented with 10% heat-inactivated FBS (Sigma), Non-Essential Amino Acids (Hyclone), Sodium Pyruvate (Hyclone), HEPES (Lonza), Beta-mercaptoethanol, Pen/Strep (Gibco), L-Glutamine (Hyclone)). Bone marrow was harvested from femur and tibia of mice by flushing bones with R10 media. Red Blood Cell lysis was performed using RBCL buffer (Invitrogen) and stopped by addition of R10 media. Cells were then filtered through 70um nylon mesh and resuspended in appropriate media.

To generate Bone Marrow-Derived Macrophages (BMDMs), cells were cultured in R10 supplemented with 30% mycoplasma-free L929 cell supernatant containing M-CSF (NCBI Biosample accession number SAMN00155972) for 5 days, with further media addition on day 3, in non-tissue culture 10 cm Petri dishes. BMDMs were detached from their plates using 5mM EDTA/PBS for use in experiments.

For Flt3L DCs, cells from one femur and tibia were cultured in 14 ml of R10 supplemented with 50ng/ml Flt3L for 9 days, with an addition of 5 ml of media on day 7. In Flt3L cultures, floating cells were harvested for use in experiments.

Peritoneal macrophages were isolated by peritoneal lavage in 10ml of PBS. Lavages were then centrifuged and plated in 10ml of R10 media in a non-tissue culture treated 10cm Petri dish and allowed to attach for 2 hours. After this time, the plates were washed with R10 to remove non-adherent cells. Remaining cells were detached with 5mM PBS/EDTA, counted and used for experiments. All experiments with peritoneal macrophages included quantification of macrophage percentage by flow cytometry.

Cell stimulation with indicated immune ligands was performed after cell counting and plating. c-di-GMP and cGAMP (Biolog) were used at 10μg/ml, 5'ppp-dsRNA (Invivogen) was used at 1μg/mg. Nucleotides were transfected into cells using LyoVEC (Invivogen) transfection reagent, following manufacturer's instructions. 100ng/ml of LPS (Invivogen), Poly(I:C) (Invivogen), 1μg/ml R848 (Invivogen), and 5μg/ml CpG DNA (Invivogen) were added directly to cell culture medium for indicated times. IFNα and IFNβ were added to cells at a concentration of 50 ng/ml and 500 U/ml, respectively.

Visualization of ER-mitochondrial contact by FRET measurements

A bicistronic FRET reporter was constructed on the lentiviral backbone pLVX-CMV2 by sequentially joining the ORFs of FRB/FKBP artificial heterodimer system partners localized to either the cytoplasmic surface of the ER (CFP-FRB-ER) or the cytoplasmic surface of the mitochondria (AKAP-FKBP-YFP), separated by a P2A protease cleavage target site. The equimolar expression of these partners allows for the estimation of ER-mitochondria extension by FRET, and the further stabilization of ER-mitochondria tethering upon addition of rapamycin, as first established by the Hajnóczky group.[64] Due to the FRB and FKBP domains in each construct, the addition of rapamycin causes rapid heterodimerization inducing tethering of membranes from two organelles that are within close proximity. This interaction was quantified by flow cytometry-based FRET assay using the Fortessa (BD Biosciences). Cells were excited with the 405nm laser to excite CFP (450/50 filter) or FRET (525/50 filter) signal. YFP signal was measured by excited cells with the 488nm laser and measuring emission with the 530/30 filter.

Efferocytosis Assays

In vitro efferocytosis assays were performed using CFSE (Invitrogen)-labelled MEFs in which apoptosis was induced by exposure to 100 mJ/cm^2 (Stratolinker) while the cells were resuspended in a small volume of PBS, followed by incubation in complete media overnight. Macrophages were plated and stimulated prior to the addition of ACs. ACs were incubated with macrophages at a ratio of 3:1 in experiments unless otherwise stated. After 1 hour, macrophages were detached for plates using 5mM EDTA/PBS and stained for macrophage specific surface markers for flow cytometry analysis. The percentage of AC$^+$ macrophages was quantified. Macrophages and ACs incubated at 4°C, as well as macrophages alone and ACs alone were used as controls.

In vivo efferocytosis assays were adapted from previously described methods.[48] In brief, mice were administered with 250 μg dexamethasone (Sigma) intraperitoneally. 4 hours later, thymic weight and cellularity was noted. Thymic macrophage numbers and thymocyte expression of Active Caspase-3 (FITC Active Caspase-3 Apoptosis Kit, BD Pharmingen # 550480) were also analyzed by flow cytometry. For bone marrow chimera experiments, chimera efficiency was determined by CD45.1/CD45.2 staining systemically and within the thymus.

Bone marrow graft

WT C57BL/6J CD45.1$^+$ mice were irradiated with 2 doses of 5.5 Gy, 3 hours apart. Irradiated mice received BM cells extracted from the medulla of indicated CD45.2+ mice using 1/10 of the total medulla from 2 femurs and 2 tibias by i.v. injection in PBS. Irradiated mice also received subcutaneous injections of 25 μg Cefovecina antibiotic per mouse in PBS. After 30 days, the reconstitution efficiency was analyzed in blood, checking the percentage of CD45.1 and CD45.2 expression in circulating monocytes and neutrophils. Successfully reconstituted mice were used for experiments.

Zymosan-induced peritonitis

As reported previously.[54,55] Briefly, mice were injected i.p. with 0.1 mg Zymosan (Invivogen). On day 11 post-injection, 4x10^6 CTV-labelled apoptotic MEFs were injected i.p. 45 minutes later, peritoneal lavage was performed with 8 ml of FACS buffer. Peritoneal exudate was surface stained and analyzed by flow cytometry.

Viral Infection and Quantification

VACV Western Reserve (VACV-WR) was a gift from Jonathan W. Yewdell and Jack R. Bennink (NIH, Bethesda, Maryland, USA). Stocks were grown in CV-1 monolayers and used as clarified sonicated cell extracts. Mice were infected i.d. in the ear with $5x10^4$ pfu of VACV-WR. On day 0, 3, or 7, ears were processed, and viral titer was quantified as previously described (Iborra et al., 2012[92]). In brief, the ventral and dorsal dermal sheets of infected mouse ears were separated with forceps, cut into fine pieces, and incubated with 50 μg/ml liberase (Roche) for 30 minutes at 37°C. Ear tissue was then filtered through a 70μm mesh. For virus titration, Homogenates were subjected to 5 freeze-thaw cycles before quantification. 100,000 CV-1 cells were plated in a 24-well culture plate overnight. The following day, media was removed from these cells and 200ul of serially diluted tissue homogenate was added to cells, in serum free DMEM media. After 1-hour incubation, DMEM with serum was added on top to prevent further viral entry. After 24 hours of incubation, supernatant was removed and the assay was stopped by fixation and staining with 0.5% crystal violet/methanol for 5 minutes. Wells were washed several times in water and left to dry. Plaques were counted and the resulting number was multiplied by the dilution factor to calculate plaque forming units (pfu)/ml.

MVA-ISG15-GG and MVA-ISG15-AA were generated as previously described.[46] BMDMs were infected with $1x10^7$ IU/ml of virus for 1 hour in DMEM-2% FBS. After 1 hour, virus containing media was removed and replaced with DMEM-10% FBS for a further 4 hours. After this time, cells were used for experiments.

Flow cytometry

For the majority of assays, cells were detached from plates using 5mM EDTA/PBS and transferred to V-bottom 96-well plates. For extracellular staining, cells were centrifuged at 1700rpm for 5 minutes and resuspended in antibody cocktails and Fc block in 50μl of FACS buffer (2.5 % FBS, 2.5 mM EDTA in PBS). Flourescence was analyzed using the LSR Fortessa (BD Biosciences) or Cytoflex LX (Beckman Coulter) and the following antibodies: CD16/CD32 (clone 2.4G2, Fc block, TonboBio #70-0161-M001), F4/80 (clone BM8)-PE (eBioscience #12-4801-82) -APC (eBioscience #17-4801-82), CD11b (clone M1/70)-eFluor660 (eBioscience #50-0112-80) -FITC (BD Pharmingen #553310), CD64 (clone X54-5/7.1)-BV421 (BioLegend #139309), CD45.1 (clone A20)-APC/Fire (BioLegend #110752), CD45.2 (clone 104)-V450 (BD Horizon #560697), Ly6A/E (Sca-1, clone D7)-PE-Cy7 (Thermo #25-5981-82). DAPI or Ghost Dye Red 780 (Cytek) were used as viability dyes depending on the experiment.

For analysis of MMP, cells were resuspended in 50 nM Tetramethylrhodamine methyl ester (TMRM; Thermo Fisher) in phenol-red free R10 media. To measure intra-organelle calcium, cells were detached from their plate by scraping, to avoid the use of calcium chelator EDTA. Cells were stained with 2μM Rhod2 probe (StemCell) in RPMI media for 20 minutes at 37°C, before washing in HBSS, DAPI was added immediately prior to analysis. F-actin and G-actin were detected following manufacturer's instructions. In brief, cells were fixed in 100μl 4% PFA for 15 minutes at room temperature. Cells were then washed 3 times in PBS and permeabilized in 1x Permeabilization buffer (eBioscience) and centrifuged at 1000g for 5 minutes. Cells were then stained in permeabilization buffer with DNase-1-AF488 (Invitrogen) and Phalloidin-Alexa647 (Molecular Probes) for 1 hour, prior to 1 wash in permeabilization buffer and 1 wash in HBSS. The geometric Mean Fluorescent Intensity (gMFI) of F-actin and G-actin staining was analyzed and the data was presented as a ratio between these values. Cytometry data was analyzed using FlowJo (TreeStar).

Confocal microscopy

Cultured BMDMs were seeded on glass coverslips at differentiation day 5 and stimulated as indicated. Cells were then washed in PBS and fixed in 4% Paraformaldehyde (Thermo Fisher) diluted in PBS for 10 minutes at room temperature, before washing in PBS. Cells were permeabilized with 0.5% Triton-X/PBS for 12 minutes at room temperature and washed in PBS. Non-specific binding was blocked by 1-hour incubation with 5% BSA/PBST (0.1%) before incubation with primary antibodies diluted 1:600 in 5% BSA/PBST overnight at 4°C. Primary antibodies against TOM20 (FL-145, Santa Cruz) and Calnexin (AF18, Santa Cruz) were used to stain mitochondria and endoplasmic reticulum, respectively. Cells were washed in PBST and incubated with fluorescently conjugated secondary antibodies (AlexaFluor488 and AlexaFluor647 conjugated anti-mouse and anti-rabbit secondary antibodies (Thermo)) diluted 1:1500 in 5% BSA/PBST and incubated for 3 hours at room temperature. Actin was decorated with an Alexa647-phalloidin conjugate (Molecular Probes). Cells were incubated with DAPI 5 minutes before the final wash step and coverslips were mounted onto frosted glass slides using ProlongGold mounting media (Life Technologies). Images were acquired using a Zeiss LSM700 confocal microscope equipped with a 40x oil objective. Images were analyzed using Fiji ImageJ software. Mitochondrial footprint and other morphological parameters were calculated using the MiNA analysis software.[38] Colocalization of two channels was highlighted using the RG2B plugin for ImageJ, and highlighted pixels within the total cellular area were quantified.

Extracellular Flux Assay

Oxygen Consumption Rate (OCR) and Extracellular Acidification Rate (ECAR) were determined by Seahorse Extracellular Flux assay (Agilent) using the MitoStress Test following the manufacturer's instructions. In brief, 100,000 BMDMs were plated in Seahorse XF96 culture plates and treated with indicated stimuli. After stimulation, media was removed from cells and replaced with Seahorse media (DMEM base media without phenol red, supplemented with 25 mM glucose, 2 mM L-glutamine, and 1 mM Sodium Pyruvate, pH 7.4). Sensor cartridges were hydrated with calibrant in a non-CO_2 37°C incubator overnight. Mitochondrial inhibitors were pipetted into the ports found in the sensor cartridge – In port A 8μM Oligomycin, in port B 9μM CCCP, in port C 10μM Rotenone and Antimycin A. Results were analyzed using Seahorse Wave software (Agilent).

Analysis of supernatant

IFN-β concentrations in supernatant were measured using LumiKine Xpress mIFN-β 2.0 (Invivogen) following manufacturer's instructions. CCL5 concentrations in supernatant were measured using a Mouse CCL5 DuoSet ELISA kit (R&D systems). Lactate was measured using L-Lactate assay kit (Sigma).

Transmission electron microscopy

Macrophages were detached from their plates in PBS-EDTA and centrifuged at 1700 rpm (5 minutes, 4°C) to form a pellet. Fixative (4% GL in 0.1M sodium cacodylate buffer (pH 7.4) and 4% paraformaldehyde) was slowly added at room temperature, so as not to disturb the pellet. After 10 minutes, cell pellet was disturbed, and cells were incubated a further 1h 50 minutes in fixative. Cells were then washed 3 times in sodium cacodylate buffer alone. A final wash in PBS with 0.01% azide was performed and pellets were kept in PBS and azide at 4°C until further sample preparation was performed. Samples were post-fixed with 1% osmium tetroxide (in dH2O) for 1 hour at room temperature, washed with dH2O and then stained with 0.5% uranyl acetate for 10 min. Samples were dehydrated in solutions of increasing alcohol content (30%, 50%, 70%, 95% and 100%) and acetone. Samples were then included in Durcupan resin and incubated at 60°C for 48 hours. 60nm sections were obtained using a Leica Ultracut S Ultramicrotome (Leica). Sections were placed in copper grids (200 mesh) and contrasted with uranyl acetate and lead citrate. Images were acquired with Jeol Jem1010 de 100 Kv electron microscope coupled with Gatan Orius SC200 digital camera. For quantification, Fiji ImageJ software was used. Adobe Photoshop and Adobe Illustrator were used for downstream image processing.

Quantitative Real-time PCR

RNA was extracted from cells using the RNeasy mini kit (Qiagen). 200ng of RNA was then reverse transcribed to cDNA using High-Capacity cDNA Reverse Transcription Kit (Thermo Fisher). cDNA was then added to a mastermix of SYBR green dye (GoTaq® qPCR, Promega) and primers targeting a gene of interest (primer sequences can be found in Table S2). SYBR green signal was measured using the CFX384 Real-Time System 384 plate reader (Bio-Rad) and analyzed using Bio-Rad CFX manager software. Normalized Ct values were calculated by normalizing target gene Ct to loading controls of the same sample (using 18S RNA expression, *Rn18s*). Fold change of gene expression was then quantified by comparing normalized Ct values to unstimulated controls, or as indicated in each individual experiment.

Western Blot

Cells were detached from plates in PBS-EDTA, washed in PBS (Gibco) and lysed in mammalian cell lysis buffer (50mM Tris-Cl pH 7.5, 1mM EDTA, 1mM EGTA, 1% (v/v) Triton X-100, 1mM sodium orthovanadate, 50mM sodium fluoride, 5mM sodium pyrophosphate, 10mM sodium β-glycerophosphate, 0.27M sucrose, 0.1% (v/v) 2-mercaptoethanol, 0.1mM PMSF, 10 μl/ml Aprotinin). Lysed samples were pre-cleared by centrifugation at 8,000 x g for 10 min. Protein was quantified in the soluble fraction using Pierce BCA Protein Assay Kit (Thermo Fisher) and desired concentrations of protein lysate were denatured by boiling in SDS sample buffer (62.5mM Tris-Cl pH 6.8, 2% (w/v) SDS, 10% Glycerol, 0.1% Bromophenol Blue, 50mM DTT). Proteins were separated by SDS-PAGE and transferred onto PVDF membranes of 0.45 μm pore (Millipore) using wet transfer (Bio-Rad). Membranes were blocked with 5% (w/v) non-fat milk, or 5% bovine serum albumin (BSA), in 0.1% Tween-20/PBS for 1 hour. Primary antibodies were used at a dilution of 1:1000 and incubated with membranes overnight at 4°C. Secondary HRP-coupled antibodies were used at 1:3000 and incubated with membranes for 3 hours at room temperature. Membranes were developed using Immobilon ECL substrate (Millipore) and imaged on the iBright FL1500 imaging system (Thermo Fisher).

Proteomics

BMDMs were obtained, as described above, from the bone marrow of C57BL/6 WT and ISG15-deficient mice (kindly provided by K. Knobeloch, Freiburg University, Germany). Cells were stimulated with recombinant IFNβ for 16 hours, then 1×10^7 cells per condition were lysed (25 mM Tris pH 8, 150 mM NaCl, 2 mM $MgCl_2$, 0.5% NP-40 and protease inhibitors) and incubated for pre-clearing with pre-washed Protein G Dynabeads (Invitrogen; 50 μl per condition; 1 hour at 4°C). 50ul of Dynabeads per condition were washed twice in 0.01% Tween PBS and resuspended in 200 μl of 0.01% Tween PBS containing 5 μg anti-ISG15 antibody (Proteintech, 15981-1-AP) per condition and incubated for 1 hour at 4°C. Pre-cleared lysates were incubated with antibody-conjugated Dynabeads (1.5 hours at 4°C). Antibody-conjugated Dynabeads were washed six times with lysis buffer and transferred to clean tubes. Protein loading buffer was added, samples were boiled at 95 °C for 5 min and samples were run on a self-poured stacking SDS-PAGE gel (10% resolving gel and 4% stacking gel) at 20 mA/gel. The electrophoresis was stopped when the front dye reaches the resolving gel, ensuring concentration of all proteins into one band. Staining was performed using Coomassie Brilliant Blue G-250 (Fermentas). Coomassie-stained gel bands were sliced and subjected to in-gel digestion. After reduction with DTT (10mM) and alkylation of Cys groups with iodoacetamide (50mM), modified porcine trypsin (Promega) was added at a final ratio of 1:20 (trypsin-protein). Digestion proceeded overnight at 37°C in 100 mM ammonium bicarbonate at pH 7.8.

Labelled peptides were loaded in buffer A (0.1% of formic acid in water (v/v)) onto a C-18 reversed phase nano-column (75 μm I.D. and 50 cm, Acclaim PepMap) and separated in a continuous acetonitrile gradient consisting of 8-31% B-solution (0.1% formic acid (v/v) in acetonitrile) for 240 min, and 50-90% B for 1 min, at a flow rate of ~200 nL/min, using an UPLC-Ultimate 3000 chromatography system (Thermo Fisher, San José, CA, USA) connected to a Q-Exactive HF mass spectrometer (Thermo Fisher). Mass spectra were acquired in a data-dependent manner, with an automatic switch between MS and MS/MS using a top 20 method. MS spectra were

acquired in a 390-1700 m/z range at 60,000 FT resolution. HCD fragmentation was performed at 33 of normalized collision energy and MS/MS spectra were analyzed at 30,000 resolution. Dynamic exclusion was set to 40 s.

For protein identification, tandem mass spectra were extracted and charge state deconvoluted by Proteome Discoverer 2.5 (Thermo Fisher Scientific). All MS/MS samples were analyzed using SEQUEST HT assuming the full trypsin digestion, two mixed cleavages allowed, and an error of 15 ppm or 0.02 Da for full MS or MS/MS spectra searches, respectively. Carbamidomethyl of C was specified as fixed modification. Oxidation in M and deamidation in Q or N were selected as dynamic modifications.

Scaffold (version Scaffold_5.2.2, Proteome Software Inc., Portland, OR) was used to validate MS/MS based peptide and protein identifications. Peptide identifications were accepted if they could be established at greater than 95,0 % probability by the Peptide Prophet algorithm[93] with Scaffold delta-mass correction. Protein identifications were accepted if they could be established at greater than 99,0 % probability and contained at least 1 identified peptide. Protein probabilities were assigned by the Protein Prophet algorithm.[94] Proteins that contained similar peptides and could not be differentiated based on MS/MS analysis alone were grouped to satisfy the principles of parsimony. Proteins sharing significant peptide evidence were grouped into clusters.

Statistical analysis

Statistical analysis was performed in Prism (GraphPad), with the details of tests performed indicated in the figure legend for each experiment.